Astron. Astrophys. 245, 371–392 (1991)

ASTRONOMY AND ASTROPHYSICS

WSRT and VLA observations of the radio galaxy B2 0326+39 at 0.6, 1.5 and 5 GHZ

A.H. Bridle[1], S.A. Baum[2], E.B. Fomalont[1], R. Fanti[3,4], P. Parma[3], and R.D. Ekers[5]

[1] National Radio Astronomy Observatory, Edgemont Road, Charlottesville, VA 22903-2475, USA
[2] Netherlands Foundation for Research in Astronomy, Postbus 2, NL-7990 AA Dwingeloo, The Netherlands
[3] Istituto di Radioastronomia, Via Irnerio 46, I-40126 Bologna, Italy
[4] Dipartimento di Astronomia dell'Università, Via Zamboni 33, I-40126 Bologna, Italy
[5] Australia Telescope National Facility, CSIRO, P.O. Box 76, Epping NSW 2121, Australia

Received August 2, accepted October 25, 1990

Abstract. The radio galaxy B2 0326+39 has been imaged with the WSRT and the VLA at 0.6, 1.5 and 5 GHz, with angular resolutions from 26″ to 0.″3. The radio source contains an unresolved opaque radio core that is linked by two jets to broad lobes with faint *S*-symmetric elongations.

The west jet is marginally brighter than the east jet on the large scale but is much brighter for the first 4 kpc from the core. The transition from "one-sided" to "two-sided" intensity symmetry between the jets is accompanied by a change in the apparent magnetic field direction on the jet axis from dominantly parallel to dominantly perpendicular to the jet. The jets do not spread (i.e., expand laterally) at a constant rate, but alternate between slow and rapid spreading. They also contain regions with both adiabatic and sub-adiabatic intensity-radius variations within 10 kpc of the core. The regions of most rapid spreading are those where the central intensity declines most slowly with increasing jet radius.

The jets do not share the *S*-symmetry of the outer steep-spectrum extensions of the lobes – the west jet has a much more pronounced "wiggle" as it enters its lobe. The spectral index of the west jet decreases by about 0.3, and the jet brightens, near an extremity of this "wiggle". The "wiggling" may therefore be related to a change in the internal structure of the jet that also stimulates relativistic particle (re)acceleration in this region.

There is evidence for a Faraday rotation measure gradient across the source, perhaps as large as 40–60 rad m^{-2}. We cannot be certain whether this gradient is intrinsic to the source or is a property of the foreground magnetoionic medium of our galaxy.

We consider various ways to estimate the Mach number and velocity of the jets. A consistent picture of the lobe energetics, jet morphology, and the polarisation properties of the jet can be found. In this picture, the jets are initially light, confined and mildly supersonic but are decelerated and become denser as they propagate away from the core. It is unlikely that the lobes have come to radiative equilibrium with the energy flux provided by the jets.

Key words: radio galaxies – jets – polarisation

1. Introduction

This paper continues a programme of imaging extended bright radio galaxies identified with radio sources from the B2 catalogue (see Colla et al. 1975 for a description of the sample). It presents images of the radio galaxy B2 0326+39 in total and polarised emission at 0.6, 1.4 and 5.0 GHz, obtained with the Westerbork Synthesis Radio Telescope (WSRT) and with the Very Large Array (VLA) of the National Radio Astronomy Observatory[1].

B2 0326+39 is identified with the bright ($m_{pg} = 14.9$, $z = 0.0243$) elliptical galaxy UGC 2755 (VV 7.08.14). A second galaxy, about two magnitudes fainter, is visible within the envelope of the identification, at a projected separation of 25″, or $\approx 8.5h^{-1}$ kpc (we use $H_0 = 100h$ km s^{-1} Mpc^{-1} throughout this paper). Table 1 lists the main optical and radio parameters of the source.

The radio source has previously been studied by Fanti et al. (1977), using the WSRT at 0.61 GHz with 54″ × 85″ resolution and at 5.0 GHz with 7.″6 × 12″ resolution. Their 0.61 GHz image showed a double-lobed structure about 6′ ($120h^{-1}$ kpc) across, centred on an unresolved core in the nucleus of VV 7.08.14. Their 5 GHz image delineated two further emission components within about 15″ of the core and placed symmetrically around it along the major axis of the larger-scale lobes. A later 1.4 GHz WSRT image at 24″ × 38″ resolution by Ekers et al. (1981) showed that the lobes have an *S* (inversion) symmetry. Images at 5 GHz with the WSRT at 6″ × 10″ resolution (Parma 1982) and with the VLA at 4.″6 × 5.″6 resolution (Bridle 1982) showed that the emission components near the core are the brightest parts of two symmetrical thin jets that join the core to the lobes.

This paper describes further radio observations that delineate the total intensity, spectral and polarisation properties of the lobes and jets in B2 0326+39 in much greater detail than before.

Send offprints requests to: P. Parma

[1] The NRAO is operated by Associated Universities, Inc., under cooperative agreement with the National Science Foundation.

Table 1. Integral properties of B2 0326+396

Optical position (α_{1950})	$03^h26^m06^s.5$
Optical position (δ_{1950})	39°37′12″
Redshift	0.0243
Distance	$72.9h^{-1}$ Mpc
m_{pg}	14.9
M_{pg}	−20.0
0.6 GHz total flux density	2.55 Jy
1.4 GHz total flux density	1.74 Jy
2.7 GHz total flux density	0.85 Jy
4.9 GHz total flux density	0.58 Jy
Total spectral index	0.8
1.4 GHz total radio luminosity	$1.1\,10^{24}h^{-2}$ W Hz^{-1}

Table 2. WSRT observational parameters

Frequency	0.6 GHz	1.4 GHz	5.0 GHz
Observing date(s)	Jan 1983	Aug 1974	Apr 1979
Observing time	12 hr	12 hr	12 hr
Interferometer spacings (meters)	72 + 72n 234 + 72n	36 + 72n	54 + 72n 234 + 72n
No. of interferometers	40	20	40
1st grating radius	46′ × 89′	10′ × 19′	6′ × 11.′6
Primary beam HPBW	84′	34′	10′

2. The observations and reductions

2.1. The WSRT data

The WSRT and its observing and data reduction procedures have been described elsewhere (Högbom & Brouw 1974; Baars & Hooghoudt 1974). Table 2 lists the relevant parameters of the WSRT for the observations reported here. The standard WSRT reduction procedure (van Someren Gréve 1974) was followed closely. The effects of sidelobes on the images of all Stokes parameters were deconvolved using the CLEAN algorithm (Högbom 1974). To compare the images at different frequencies, we made 5 GHz images convolved to the resolution of those at 1.4 and at 0.6 GHz. These images, restored in the CLEAN procedure using identical Gaussian beams at all frequencies, are termed "low resolution WSRT images" below. Details of them are given in Table 3.

2.2. The VLA data

The VLA and its observational and data reduction techniques have been described by Thompson et al. (1980) and by Napier et al. (1983). Our observations were made in nonstandard VLA configurations whose relevant parameters are given in Table 4. Note especially that the VLA configuration at the time of the 1.5 GHz observations contained only 15 working antennas, but also that both the 1.5 GHz and 4.9 GHz configurations provided a much wider range of baselines than a single "standard" (A, B, C, D) VLA configuration. In particular, the 1.5 GHz data provide a maximum fringe separation of 31′ and have at least 50% sensitivity to circular Gaussian components with FWHM up to about 14′. The 4.9 GHz data have a maximum fringe separation of 8.′6 and at least 50% sensitivity to circular Gaussian components with FWHM up to 3.′8.

The flux density and polarisation position angle scales for the VLA observations were calibrated by observing 3C 286. We assume that 3C 286 has flux densities of 14.5 Jy and 7.41 Jy at 1.5 and 4.9 GHz and an integrated polarisation position angle of 33° at both frequencies. The position scale was calibrated relative to the unresolved core of 3C 84, assumed to be at $\alpha(1950.0) = 03^h\,16^m\,29^s.569$, $\delta(1950.0) = +41°19'51''.94$. The on-axis instrumental polarisations of the antennas were calibrated to within a few tenths of one percent by observing 3C 84 over a wide range of parallactic angles at each frequency.

The images were analysed with the NRAO "AIPS" software, using W.D. Cotton's ungridded-subtraction algorithm "MX" for imaging and CLEANing. The effects of amplitude and phase uncertainties of atmospheric and instrumental origin were minimised by iterative use of Schwab's (1980) self-calibration algorithm, using CLEAN components as the input models.

The 1.5 GHz data were significantly confused by several background sources far from the delay tracking and visibility averaging centre. Inexact CLEANing of the sidelobe reponses to these sources limits the dynamic range on most of the final 1.5 GHz VLA images to about 100:1.

Table 5 summarises pertinent details of the VLA images.

Table 3. WSRT map parameters

Frequency (GHz)	Beam FWHM (arcsec, $\alpha \times \delta$)	Interferometer spacings shortest/incr./longest	Rms noise (mJy)	Zero offset (mJy)
5.0	6 × 10	900/600/26690λ	0.5	−0.2
5.0	26 × 41	900/600/6900λ	0.8	−0.5
1.4	26 × 41	857/343/6686λ	0.8	−1.7
1.4	26 × 41	172/343/6686λ	0.8	−1.5
0.6	26 × 41	147/147/5437λ	1.2I 0.5U, Q	−0.1

Table 4. VLA observational parameters

Frequency	1.465 GHz	4.885 GHz
Observing date	14 July 1979	15 April 1980
Observing time	12 hr	12 hr
Bandwidth	50 MHz	50 MHz
Antenna stations	W 8, 16, 24, 32, 40, 56, 64	W 8, 10, 16, 24, 32, 40, 48, 56, 64
	E 3, 4, 12, 16, 18	E 1, 2, 3, 4, 8, 12, 18, 24, 48
	N 2, 4, 6	N 2, 4, 6, 8, 14, 18, 32, 40
Shortest proj. spacing	110λ	400λ
Longest spacing	87 500λ	400 000λ
No. of interferometers	105	325
Primary beam HPBW	31′	9′.2

Table 5. VLA map parameters

Frequency (GHz)	Beam FWHM (arcsec, $\alpha \times \delta$)	Taper (kλ)	Rms noise (μJy)	Zero offset (μJy)	Flux (Jy) at $u, v = 0$
1.465	6 × 10	56 × 14	*I* 320E/420W *QU* 130E/130W	+200	1.8
1.465	4 × 4	72	*I* 160 *QU* 95	+40	1.8
4.885	6 × 10	22 × 15	*IQU* 130	+60	0.58
4.885	4 × 4	37 × 42	*IQU* 70	+23	0.58
4.885	2 × 2	100	*IQU* 45	−5	0.58
4.885	0.6 × 0.6	none	*IQU* 40	+10	0.58

Notes: The rms noise in the 6″ × 10″ data at 1.465 GHz is dominated by responses to a confusing source to the south-west; the rms is therefore given separately for the East (E) and West (W) halves of the field.

3. Imaging

This section describes selected images in order of increasing resolution and frequency, to document the principal structural features of the source on successively smaller angular scales.

3.1. 0.61-GHz WSRT data at 26″ × 41″ resolution

These data were taken in the expanded WSRT configuration with 40 interferometers and 3 km maximum baseline. Figure 1 shows the total intensity distribution. The source has a triple structure ~7′ (~$140h^{-1}$ kpc) in overall extent with broad outer components. The east and west lobes have faint ***S***-symmetric extensions for about 3′ ($60h^{-1}$ kpc) towards the north-east and 2′.5 ($50h^{-1}$ kpc) towards the south-west respectively. The most extended emission in this source therefore has a rough ***S*** (inversion) symmetry.

Figure 2 shows the linearly polarised intensity $P = \sqrt{Q^2 + U^2}$ and position angle represented as ***E*** vectors superposed on selected total intensity contours from Fig. 1. The central

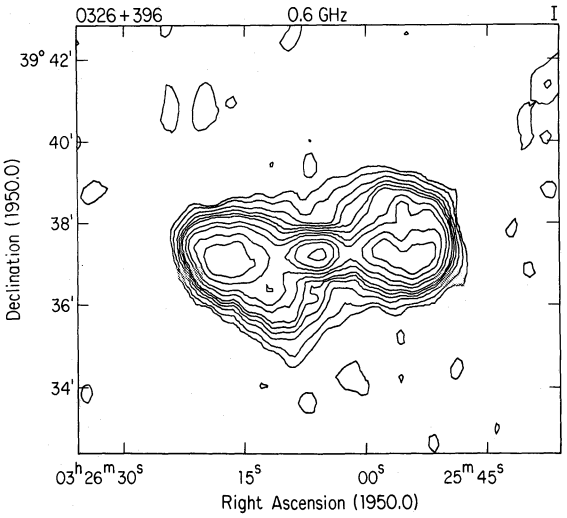

Fig. 1. Total intensity (Stokes *I*) distribution at 608.5 MHz, from the WSRT data at 26″ × 41″ resolution. Contours are drawn at 2, 4, 8, 12, 16, 20, 30, 40, 60, 80 and 120 mJy per CLEAN beam

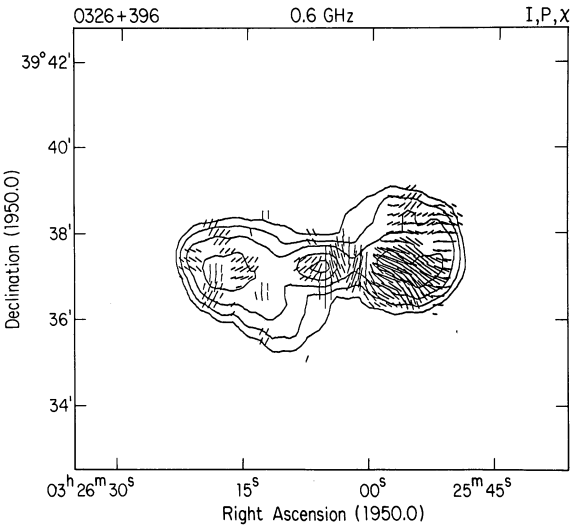

Fig. 2. *E* vector distribution (polarised intensity P, position angle χ) at 608.5 MHz, from the WSRT data at 26″ × 41″ resolution, superposed on I contours at 8, 20, 40, 80 and 120 mJy per CLEAN beam

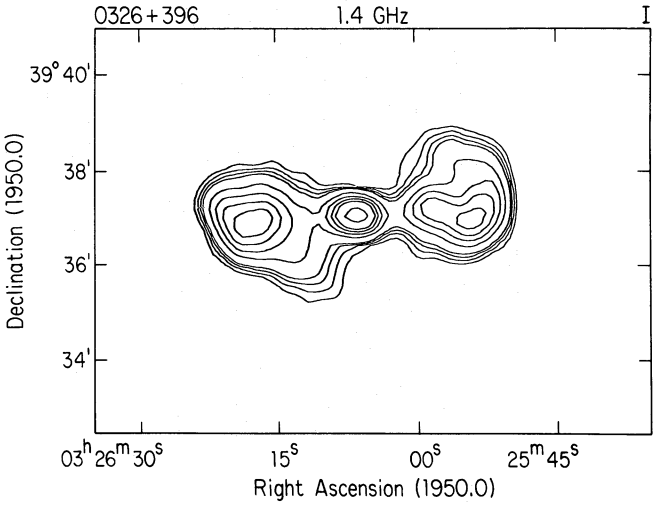

Fig. 3. Total intensity (Stokes I) distribution at 1.4 GHz, from the WSRT data at 26″ × 41″ resolution. Contours are drawn at 10, 15, 20, 30, 40 and 60 mJy per CLEAN beam

"component", which at this resolution contains the unresolved core and the bases of the two bright jets (see Sects. 3.3 and 3.4 below) has a 0.6-GHz degree of linear polarisation $p_{0.6} = P/I \sim 0.02$ to 0.05. The west lobe has $p_{0.6}$ up to 0.1, with a minimum near the centre of the lobe and maxima toward its edges. The east lobe has significantly lower linear polarisation at this frequency ($p_{0.6} < 0.03$ to 0.04).

3.2. 1.4-GHz WSRT data at 26″ × 41″ resolution

These data, taken in the older WSRT configuration with 1.4 km maximum baseline, are shown in Figs. 3 (total intensity) and 4 (linear polarisation vectors). The central "component", which is extended by $\approx 40''$ in p.a. 90° at this frequency, again exhibits significant net linear polarisation ($p_{1.4} \sim 0.05$ to 0.12), while the lobes are more strongly polarised, with $p_{1.4}$ reaching 0.2. At this frequency, the ***E*** vectors in the broad components have a regular pattern that suggests that the large-scale magnetic field in the lobes is well organised. As at 0.61 GHz, the degree of polarisation has a minimum ($p_{1.4} \sim 0.05$) near the centre of the west lobe, and maxima ($p_{1.4} \sim 0.15$ to 0.2) near its edges.

3.3. 4.9-GHz total intensity data at 6″ × 10″ resolution

Figure 5 displays the total intensity over most of the source at 6″ × 10″ ($2h^{-1} \times 3.4h^{-1}$ kpc) resolution from the VLA data at 4.9 GHz. This resolution was chosen to match that of the WSRT data at this frequency previously shown by Parma (1982). The jets are unresolved in the North-South direction at this resolution until they enter the lobes. The VLA and WSRT data agree well, allowing for their differing sensitivities. They separate the central "component" of the WSRT image in Fig. 3 into an unresolved core and the bright bases of two jets. These jet bases are the components first detected at 5 GHz by Fanti et al. (1977). An unresolved core is still partly blended with the bases of the jets at this resolution.

The west jet leaves the core in p.a. −93° at this resolution, then bends northward to p.a. −83° before entering the west lobe. It deflects southward again after a bright spot, then connects to what appeared to be the bright southern rim of the west lobe in Fig. 3. Figure 5 suggests that the faint extension of the west lobe towards the north-east is a weak continuation of the jet round the outer edge of this lobe.

The structure in the east lobe differs qualitatively from that in the west lobe. The east jet ends in a diffuse patch whose brightest region is roughly opposite a similar peak in the west jet; both of these features are south of the core, and could therefore be described as having ***C*** symmetry relative to the core. The paths of the two jets between the core and these features are markedly different, however. The east jet enters the east lobe on a path that lacks a counterpart of the large bend in the west jet near $\Theta = 90''$.

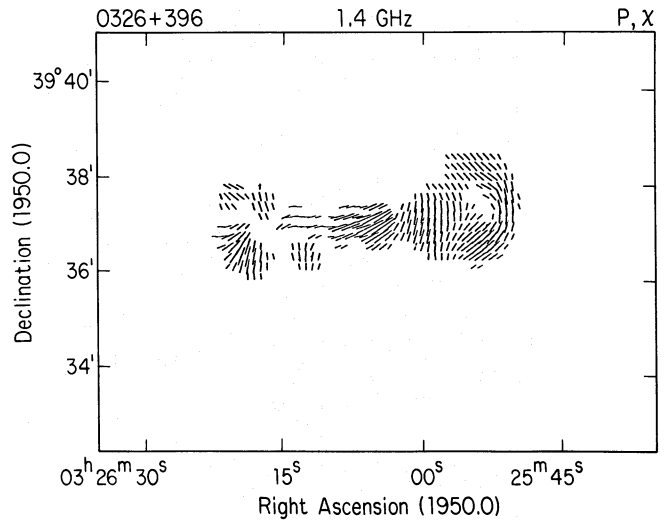

Fig. 4. *E* vector distribution (polarised intensity P, position angle χ) at 1.4 GHz, from the WSRT data 26″ × 41″ resolution

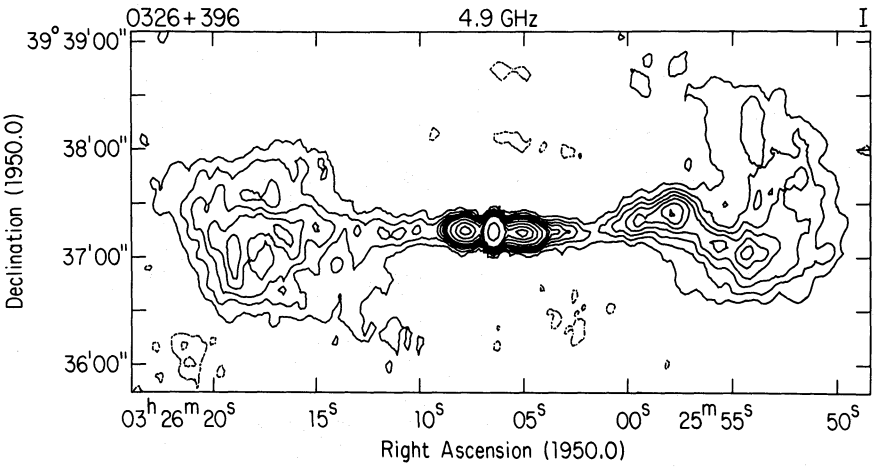

Fig. 5. Total intensity (Stokes I) distribution at 4.885 GHz, from the VLA data at 6″ × 10″ resolution. Contours are drawn at −0.8, −0.4, 0.8, 1.2, 1.6, 2, 2.4, 2.8, 4, 6, 8, 10 and 38.8 mJy per CLEAN beam. The last contour (in the centre of the core) shows the FWHM of the CLEAN beam

The east jet does not clearly connect to the asymmetric extension of its lobe, unlike the west jet. The rough ***S*** symmetry of the outer extensions of the lobes is therefore not accompanied by similar ***S*** symmetry in the jets.

3.4. 1.5 and 4.9 GHz polarisation data at 4″ resolution

Figure 6 shows the distribution of the 1.5-GHz (a) and 4.9-GHz (b) linear polarisations over the first 40″ ($13.6h^{-1}$ kpc) at 4″ resolution. The integrated polarisation of the "central component" in the 1.4-GHz WSRT data arises from bright emission regions at the bases of the two jets that have $p_{1.5}$ between 0.25 and 0.35. The apparent polarisation of the WSRT "central component" is the result of blending this jet emission with emission from the unresolved core which has $p_{1.5} < 0.01$ (5 GHz) and with emission from the first 5″ of the west jet, where the ***E*** vectors are rotated through about 90° from the orientation that dominates further out. The degrees of linear polarisation $p_{4.9}$ observed with the VLA are slightly higher at this resolution – from 0.25 to nearly 0.4 – but at most positions in the jet the depolarisation ratio $D_{4.9}^{1.5} = p_{1.5}/p_{4.9}$ between 1.5 and 4.9 GHz is within errors of unity.

3.5. 4.9-GHz VLA data at 2″ resolution

Figure 7a shows the total intensity distribution over the first 40″ ($13.6h^{-1}$ kpc) of the jets at 2″ ($680h^{-1}$ pc) resolution from the 4.9-GHz VLA) data. The brightness asymmetry between the first ~5″ ($1.7h^{-1}$ kpc) of the east and west jets is clear at this

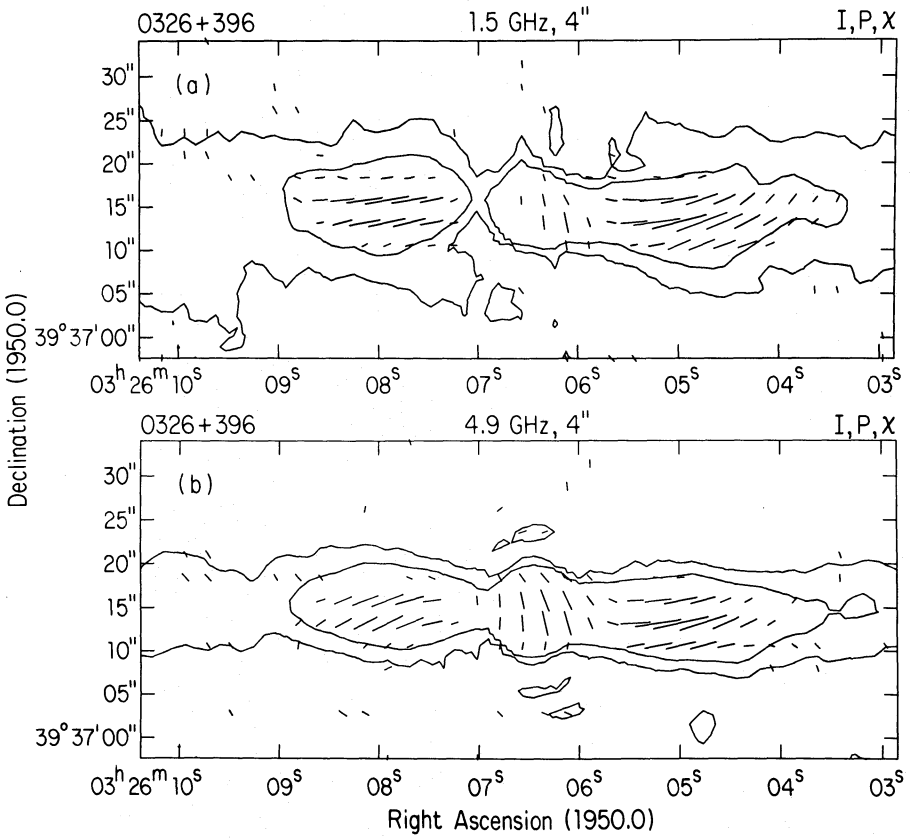

Fig. 6. a ***E*** vector distribution (polarised intensity P, position angle χ) at 1.465 GHz and **b** ***E*** vector distribution at 4.885 GHz, from the VLA data at 4″ × 4″ resolution. The vectors are superposed on I contours at 0.5 and 2 mJy per CLEAN beam in **a** and 0.225 and 0.9 mJy per CLEAN beam in **b**. A vector of length 1″ on the angular scale corresponds to $P = 0.53$ mJy per CLEAN beam in **a**, and 0.33 mJy per CLEAN beam in **b**

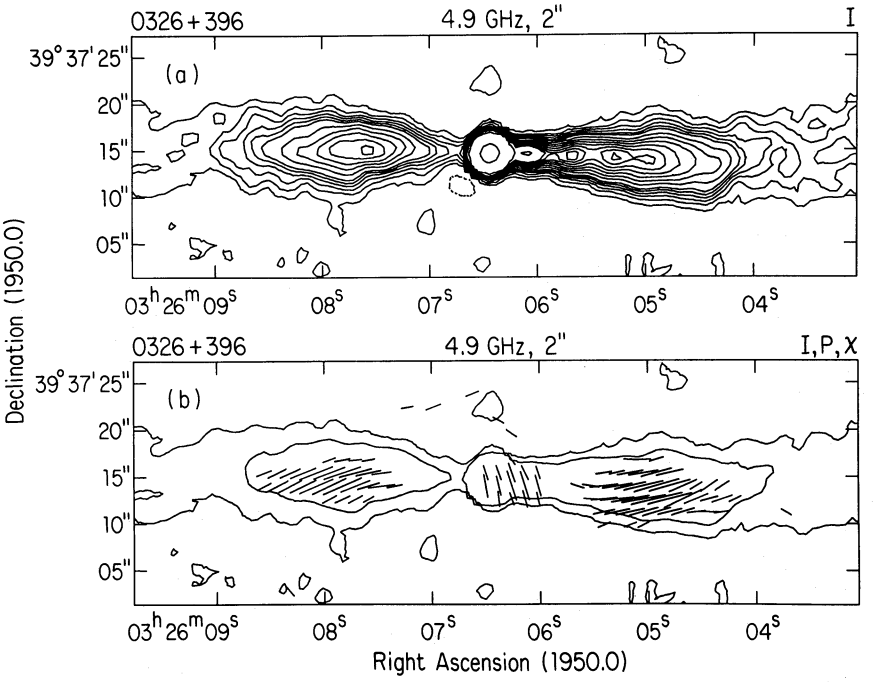

Fig. 7. a Total intensity (Stokes *I*) distribution and **b** ***E*** vector distribution (polarised intensity *P*, position angle χ) from the 4.885-GHz VLA data at 2″ × 2″ resolution. *I* contours at −0.1, 0.1, 0.2, 0.3, 0.4, 0.5, 0.6, 0.8, 1, 1.2, 1.4, 1.6, 1.8, 2, 3 and 38.09 mJy per CLEAN beam (**a**) and 0.1 and 0.4 mJy per CLEAN beam (**b**). The contour in the centre of the core on **a** shows the FWHM of the CLEAN beam. In **b**, a vector of length 1″ on the angular scale corresponds to $P = 0.16$ mJy per CLEAN beam

resolution – the first 5″ of the west jet is from 7 to 25 times brighter than the corresponding region of the east jet, depending on where they are compared. The west jet has a brightness "plateau" on which the central intensity declines slowly between 5″ and about 18″ from the core. The east jet reaches its maximum brightness near the middle of this range on the other side of the core. The jet structure is therefore "one-sided" by Bridle's (1984) definition *at its base*, but becomes "two-sided" about 10″ from the core.

The change in the brightness symmetry of the jets is accompanied by a change in the orientation of the linear polarisation of the west jet, as shown in Fig. 7b. In the first 5″ ($1.7h^{-1}$ kpc), the 4.9-GHz ***E*** vectors are roughly perpendicular to the ridge line of the jet, while for about 15″ ($5h^{-1}$ kpc) beyond that they are roughly parallel to it. This behaviour resembles that found in 3C 31 by Fomalont et al. (1980), where the northern jet has a bright "one-sided" base polarised with ***E*** perpendicular to the jet ridge, followed by a long region with ***E*** parallel to the jet ridge.

Figure 8 shows a profile of the total intensity along a line passing through the peak of the core and through the brightness maxima of the two jets ∼15″ from the core. The brightness asymmetry between the jets in the first 10″ is clearly evident.

3.6. 4.9-GHz VLA data at maximum resolution

Figure 9 displays the 4.9-GHz total intensity over the first 20″ of each jet at 0.″6 ($203h^{-1}$ pc) resolution. It also shows the strong brightness asymmetry between the bases of the two jets. A region of reduced intensity, ∼2″ ($680h^{-1}$ pc) long, is also apparent between the unresolved core and the first bright knots at the base of the west jet. The polarised signal at this resolution is too weak to be displayed with adequate signal to noise.

Figure 10a shows more detail of the "one-sided" bright knots at the base of the west jet, within 7″ ($2.4h^{-1}$ kpc) of the core. The knots are resolved along the jet axis. The brightest feature is at the coreward side of the second knot, 3.″8 ($1.3h^{-1}$ kpc) from the core. Figure 10b shows a Maximum Entropy Method deconvolution of the same region, smoothed with a 0.″3 circular Gaussian beam – the maximum resolution that can be obtained reliably with our data. This image suggests that the base of the jet contains two narrow knots about 0.″5 apart followed by a sudden widening at the brightest feature. The mean position angle of the ridge line is close to −90° until this feature. Both the CLEAN (Figs. 9 and 10a) and MEM deconvolutions (Fig. 10b) show that, beyond this brightest feature, the ridge line of the jet deflects to the south then oscillates around a mean position angle of −92.°3. The oscillation "wavelength" is ill-defined, but of order of $\lambda \approx 2.''5$.

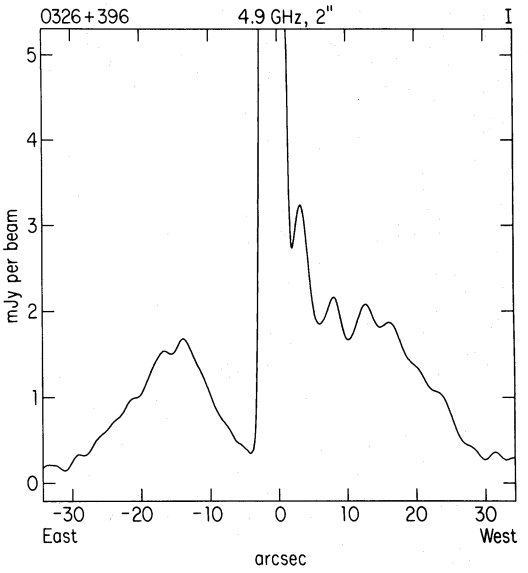

Fig. 8. Profile of total intensity *I* in p.a. −92.°3 through the peak of the core, from the VLA data at 2″ resolution

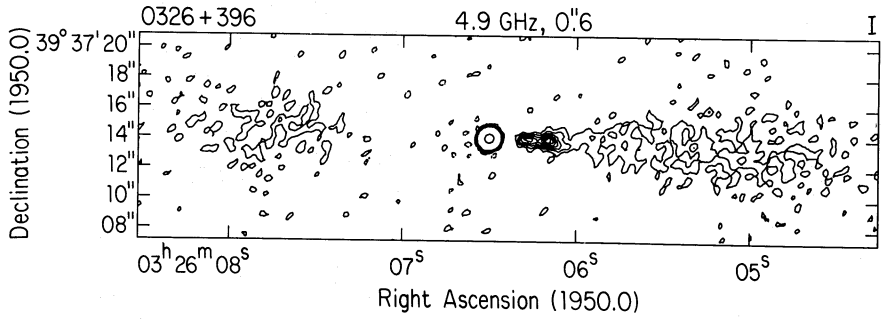

Fig. 9. Total intensity distribution at 4.885 GHz, VLA data at 0".6 by 0".6 resolution. Contours at −0.1, 0.1, 0.2, 0.3, 0.4, 0.5, 0.6, 0.7, 0.8 and 39.05 mJy per CLEAN beam. The contour in the centre of the core shows the FWHM of the CLEAN beam

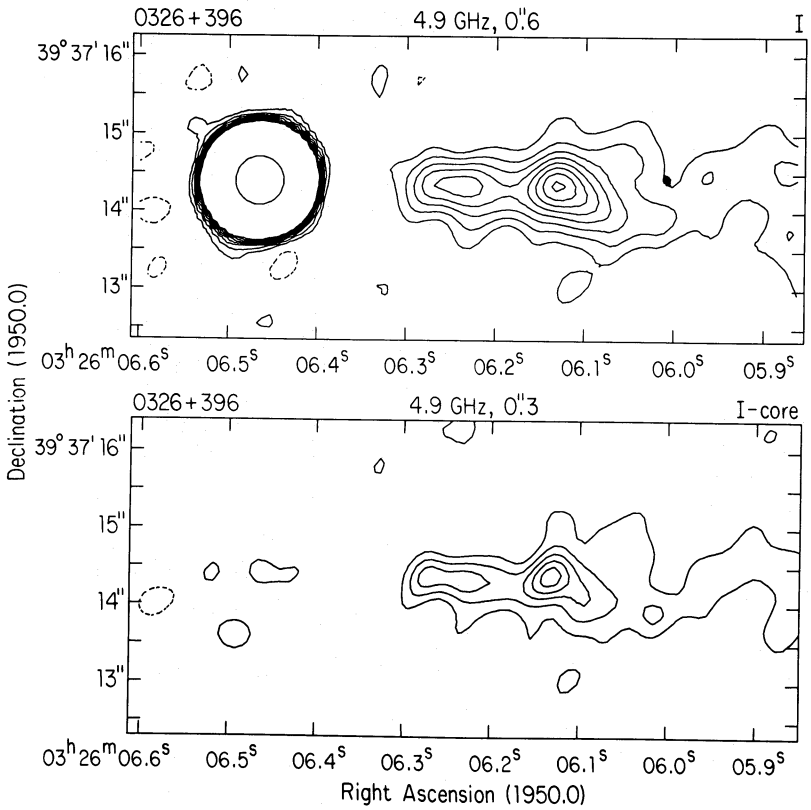

Fig. 10. (*upper*) An expanded plot of the inner region of Fig. 9, to show the knot structure clearly. (*lower*) MEM image at 0".3 resolution, to show finer detail in the inner knots – the unresolved core has been subtracted from this image

Note that the region shown in Fig. 10 is about as long (in projection) as the entire one-sided optical/radio jet in M 87 (Virgo A), which shows a similar sequence of features.

4. The radio core

Table 6 summarises parameters of the core derived from the WSRT and VLA data. The spectral index is obtained by comparing the VLA 1.5 GHz data (July 1979) with the WSRT 5.0 GHz data (April 1979). Although the core is better separated from the bases of the jets in the high-resolution VLA data, the VLA data were obtained almost a year after the WSRT data, so the core may have varied in intensity. The image at 6" × 10" resolution derived from the VLA 4.9 GHz data yields the same value for the core flux density (78 mJy) as the image from the same data at 0".6 resolution, showing that the lower-resolution estimate of the core flux density at this frequency is not contaminated by blending with the bases of the jets. The difference between the core flux density estimated from the April 1979 5.0 GHz WSRT data and the April 1980 4.9 GHz VLA data at the same resolution instead suggests that the core decreased in intensity by about 20 mJy near 5 GHz between April 1979 and April 1980.

Table 6. Core Properties of B2 0326+396

4.9 GHz VLA position (α_{1950})	$03^h26^m06^s.5$
4.9 GHz VLA position (δ_{1950})	39°37'14"
1.5 GHz flux density (VLA)	50 mJy
5.0 GHz flux density (WSRT)	98 mJy
Spectral index	−0.55
Angular size	≤0".05
1.4 GHz luminosity	$3.6\,10^{22}h^{-2}$ W Hz^{-1}

The luminosity of the core at 5 GHz is $\sim 5h^{-2}\ 10^{22}$ W Hz^{-1}, which is normal for a radio galaxy of this total power ($1.1h^{-2}\ 10^{24}$ W Hz^{-1}) at 1.4 GHz (Feretti et al. 1984). The degree of linear polarisation of the unresolved core at 5 GHz is $p_5 < 0.004$, con-

sistent with zero to within the uncertainties in the instrumental calibration.

5. The jets

5.1. Collimation properties

The observed jet FWHMs Φ_0 were determined at 0".6, 2" and 4" resolution by fitting Gaussians to transverse cuts across the VLA *I* images at 4.9 GHz. The transverse brightness profiles of the jets are center-brightened and are satisfactorily fitted by Gaussians over most of their length. Figure 11a shows the varition of the *deconvolved* FWHMs, $\Phi = \sqrt{(\Phi_0^2 - \Phi_b^2)}$, where Φ_b is the FWHM of the CLEAN beam, plotted against Θ, the angle from the core, over the range $-100'' < \Theta < +150''$. Figure 11b shows the same data over the range $-35'' < \Theta < 40''$. The noise in the estimates of Φ changes with the brightness of the jets, and is estimated by the scatter among *adjacent* points in these plots. The deconvolved values of Φ measured at different resolutions agree well, showing that these estimates are not discernibly biased by the beam deconvolution (which was usually restricted to the range $\Phi/\Phi_b > 0.5$).

The jets spread irregularly, i.e. Φ does not increase linearly with Θ over the whole range of Θ. The *mean* spreading rate $\overline{d\Phi/d\Theta}$ over the whole 140" ($47h^{-1}$ kpc) length of the west jet is 0.21 ± 0.01. This mean rate is normal for sources with this total power (Bridle 1984, 1986; Parma et al. 1987) but both jets have regions that deviate significantly from the mean rate, particularly in their inner 40" ($14h^{-1}$ kpc). Irregular spreading of jets is common in radio galaxies (e.g. Perley et al. 1979; Bridle et al. 1980; Willis et al. 1981; Fanti et al. 1982; Saunders et al. 1982; Burns et al. 1983; Perley et al. 1984; Killeen et al. 1986; O'Dea & Owen 1986; Morganti et al. 1987) – *no well-resolved jet in a radio galaxy spreads at the steady rate expected of a free (ballistic) jet.*

We therefore combine the brightness and spreading properties of the west jet to partition both jets into five regions for further discussion (see Table 7).

Region (1) extends from the core to $\Theta = 5''$ ($1.7h^{-1}$ kpc) where the west jet contains its initial series of bright knots. The jet first becomes detectable at $\Theta = 3''$ ($1h^{-1}$ kpc from the core). Although its mean spreading rate in region (1) is $\overline{d\Phi/d\Theta} = 0.41 \pm 0.06$, the $\Phi(\Theta)$ data extrapolate to $\Phi = 0$ for $\Theta > 0$. This non-zero intercept suggests that the jet spreads more slowly within $1h^{-1}$ kpc of the core. There is, indeed, a hint of slower spreading in the data near $\Theta = 3''$ (see Fig. 11 and the MEM image in Fig. 10b).

Region (2) exhibits slow decreases in the central intensity and in the spreading rate. We take the end of the slow brightness decrease and the onset of the "pause" in the jet spreading to mark the end of this region at $\Theta = 18''$ ($6.1h^{-1}$ kpc).

Region (3) is characterised by a "recollimation shoulder" in the lateral expansion of the west jet, which continues until $\Theta \approx 40''$ ($14h^{-1}$ kpc); the mean spreading rate for $18'' < \Theta < 40''$ is only 0.10 ± 0.02.

In region (4), the west jet again spreads more rapidly. From its collimation properties alone, region (4) could encompass the rest of the detectable jet. Both the central intensity and the integrated intensity per unit length increase rapidly near the first major bend in the jet, however. We adopt $\Theta = 90''$ ($31h^{-1}$ kpc), just before this bend, as the end of region (4).

Region (5) contains the bright, sharply curved segment of the jet in the west lobe. Having thus subdivided the outer jet by its

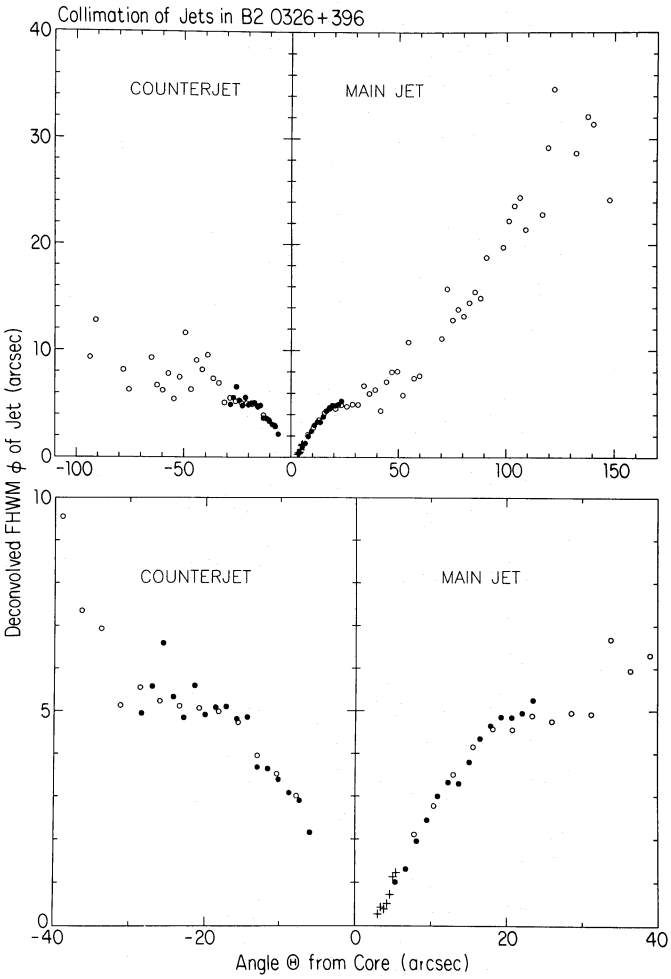

Fig. 11. Collimation (spreading) of the jets from the VLA data at 4.885 GHz. Crosses – data at 0".6 resolution; filled circles – data at 2" resolution; open circles – data at 4" resolution. The deconvolved jet FWHM Φ obtained from Gaussian fitting of the transverse jet profiles is plotted against the angle Θ from the core at the maximum of the profile. (Upper panel – data for all Θ at which the errors in Φ are $<10\%$; lower panel – data for $-40'' < \Theta < +40''$ only)

brightness characteristics, we find that the spreading rate is marginally lower in region (4) before the bend (0.22 ± 0.03) than in region (5) after it (0.28 ± 0.05).

The east jet is undetectable in region (1) and reaches its peak central intensity midway through region (2). The spreading rates of the two jets are similar throughout regions (2) and (3). Beyond about 40" ($14h^{-1}$ kpc) from the core, the east jet expands more slowly than the west jet, and becomes relatively fainter. Region (5) has no clear counterpart in the east jet, which becomes difficult to trace against its lobe beyond $\Theta = -90''$.

5.2. Intensity-radius and field strength evolution

Figure 12 plots the deconvolved central intensity *I* logarithmically against the deconvolved FWHM Φ for both jets. The deconvolved intensities were derived from the observed central intensities I_0 using the relation for Gaussian profiles, i.e.

$$\left(\frac{I}{I_0}\right)^2 = \frac{\Phi^2 + \Phi_b^2}{\Phi^2}. \quad (1)$$

Table 7. Parameters of principal jet regions

Region	$0'' < \Theta \leq 5''$	$5'' < \Theta \leq 18''$	$18'' < \Theta < 40''$	$40'' < \Theta \leq 90''$	$90'' < \Theta \leq 140''$
Distance (kpc)	0 to $1.7h^{-1}$	$1.7h^{-1}$ to $6.1h^{-1}$	$6.1h^{-1}$ to $14h^{-1}$	$14h^{-1}$ to $31h^{-1}$	$31h^{-1}$ to $47h^{-1}$
West jet					
$\langle d\Phi/d\Theta \rangle$	$+0.41 \pm 0.06$	$+0.28 \pm 0.01$	$+0.10 \pm 0.02$	$+0.22 \pm 0.03$	$+0.28 \pm 0.05$
$I \propto \Phi^n$, $n =$	-0.92 ± 0.22	-0.61 ± 0.07	-4.40 ± 1.10	$+0.00 \pm 0.18$	-0.41 ± 0.30
$B_{eq} \propto \Phi^m$, $m =$	-0.54 ± 0.06	-0.46 ± 0.02	-1.55 ± 0.32	-0.28 ± 0.05	-0.40 ± 0.08
$U_{eq} \propto \Theta^p$, $p =$	-2.72 ± 0.58	-1.13 ± 0.10	-1.94 ± 0.15	-0.72 ± 0.21	-1.03 ± 0.23
$\langle \alpha_{4.9}^{1.5} \rangle$, 4″ beam		$+0.53 \pm 0.01$	$+0.49 \pm 0.02$	$+0.72 \pm 0.04$	$+0.57 \pm 0.04$
$\langle \alpha_{4.9}^{1.5} \rangle$, 6″ beam		$+0.54 \pm 0.01$	$+0.63 \pm 0.02$	$+0.87 \pm 0.04$	$+0.60 \pm 0.04$
$S_{4.9}^{int}$, mJy	3.4	27	16	22	46
$S_{1.5}^{int}$, mJy		51	34	63	95
Magnetic config	$B_{\parallel}$	$B_{\perp}$	Oblique		
East jet					
$\langle d\Phi/d\Theta \rangle$		$+0.25 \pm 0.02$	$+0.18 \pm 0.04$	$+0.04 \pm 0.04$	
$I \propto \Phi^n$, $n =$		$+0.77 \pm 0.27$	-2.92 ± 1.00	$+0.05 \pm 0.40$	
$B_{eq} \propto \Phi^m$, $m =$		-0.02 ± 0.08	-1.12 ± 0.29	-0.27 ± 0.11	
$U_{eq} \propto \Theta^p$, $p =$		$+0.03 \pm 0.12$	-2.38 ± 0.08	-0.57 ± 0.24	
$\langle \alpha_{4.9}^{1.5} \rangle$, 4″ beam		$+0.49 \pm 0.01$	$+0.70 \pm 0.03$	$+0.69 \pm 0.05$	
$\langle \alpha_{4.9}^{1.5} \rangle$, 6″ beam		$+0.57 \pm 0.01$	$+0.78 \pm 0.03$	$+0.86 \pm 0.03$	
$S_{4.9}^{int}$, mJy		19	14	13	
$S_{1.5}^{int}$, mJy		38	35	37	
Sidedness (6 cm)		1.42:1	1.14:1	1.65:1	
Sidedness (20 cm)		1.34:1	0.97:1	1.70:1	

The first four jet regions defined above are clearly separated in Fig. 12. In terms of $\log_{10}\Phi$, their boundaries are:

(1): $-0.6 < \log_{10}\Phi < 0.05$, where $I \propto \Phi^{-0.92 \pm 0.22}$,

(2): $0.05 < \log_{10}\Phi < 0.65$, where the intensity falls less rapidly, with $I \propto \Phi^{-0.61 \pm 0.07}$,

(3): $0.65 < \log_{10}\Phi < 0.8$, where the intensity declines rapidly while the jet expands slowly and $I \propto \Phi^{-4.4 \pm 1.1}$, and

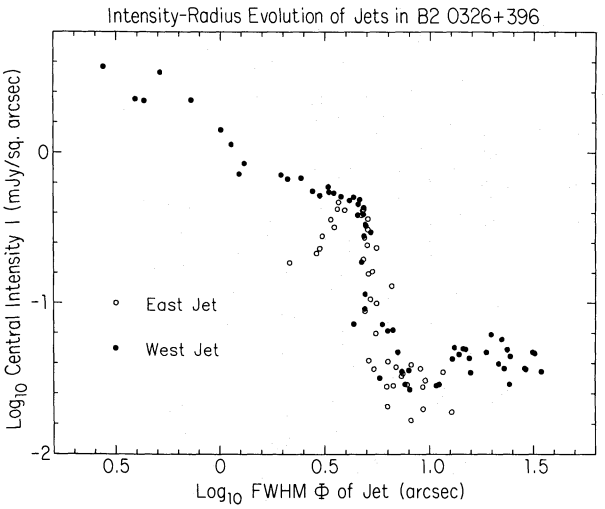

Fig. 12. Logarithmic plot of the maximum intensity in the transverse profile of the jet versus the FWHM of the profile, both quantities being deconvolved from the data assuming Gaussian profiles. The intensity data at different resolutions have been normalised by the Gaussian beam areas; the data from the three different VLA resolutions used in Figure 11 overlap within the errors due to noise, so are not distinguished here

(4) + (5): $0.8 < \log_{10}\Phi < 1.6$, where there is much scatter in the $I(\Phi)$ relation.

As noted above, the east jet is undetectable in the equivalent of region (1) but *brightens* rapidly as it spreads in region (2). The fastest brightening has $I \propto \Phi^{2.5 \pm 0.4}$. In regions (3) and beyond the properties of the east jet are similar to that of the west jet, until it becomes hard to trace against the east lobe.

Apart from the slowly varying effect of the spectral index gradient, the equipartition magnetic field strength $B_{eq} \propto (I/\Phi)^{2/7}$, so the evolution of $\log_{10} B_{eq}$ with $\log_{10}\Phi$ (Fig. 13) necessarily exhibits the same principal regions as the $I(\Phi)$ data. In this plot, regions (1) and (2) are less clearly distinguishable and the whole range $-0.6 < \log_{10}\Phi < 0.65$ (the first 18″, or $6.1h^{-1}$ kpc, of the jet) is reasonably well fitted by $B_{eq} \propto \Phi^{-0.51 \pm 0.03}$. In the slowly-expanding region (3) $B_{eq} \propto \Phi^{-1.55 \pm 0.32}$, while in the re-expansion beyond this (4) B_{eq} again declines more slowly with Φ.

5.3. *Minimum energy density and pressure*

The equipartition energy density U_{eq} and the minimum pressure p_{min} are both proportional to B_{eq}^2, or $(I/\Phi)^{4/7}$, apart from the (generally slow) variation of the spectral index. Figure 14 plots $\log_{10}(U_{eq})$ against $\log_{10}\Theta$ to show how the equipartition energy density falls with distance from the core. The intensity ratio between the jets produces a small displacement between the two curves in this Figure. The power law exponents of the $U_{eq}(\Theta)$ variation in the five main jet regions are listed in Table 7, our choice of boundaries between these regions emphasises the fluctuations in this exponent. Figure 14 shows that after the steep ($\Theta^{-2.7}$) decline in region (1) of the west jet, and the "turning on" of the east jet, the data for both jets can be described adequately

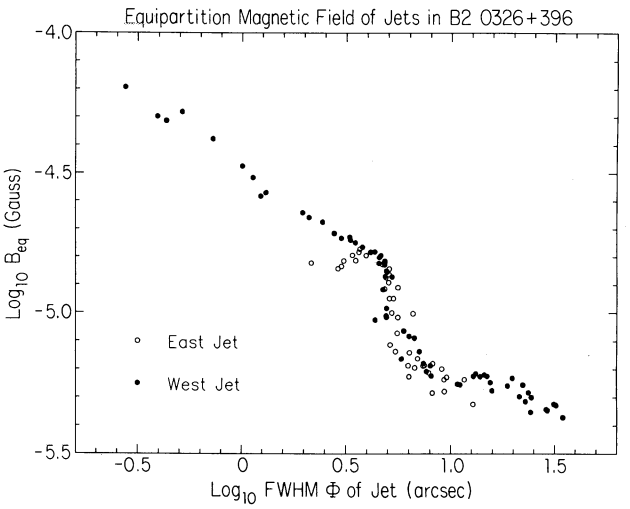

Fig. 13. Logarithmic plot of the equipartition magnetic field strength (in gauss) against deconvolved FWHM Φ of the west jet (filled circles) and east jet (open circles), combining VLA data from all three resolutions shown in Fig. 11

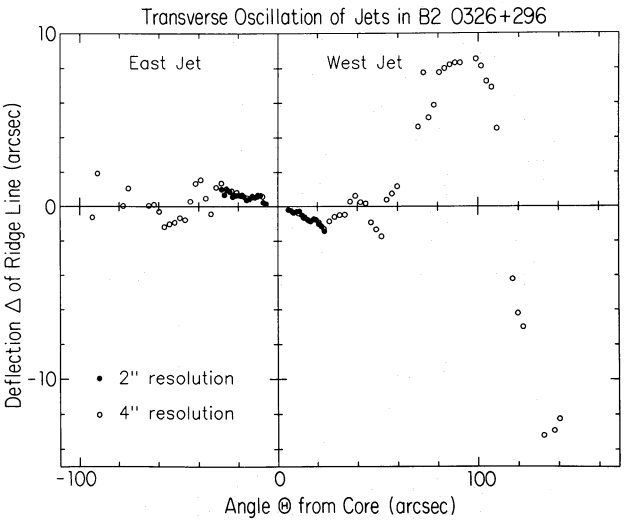

Fig. 15. Deflection Δ of the peaks in the transverse intensity profiles of the jets from an east-west line through peak of the core source, plotted against angle Θ from the core, to show the lateral oscillation ("wiggle"). (Filled circles – data at 2″ resolution; open circles – data at 4″ resolution)

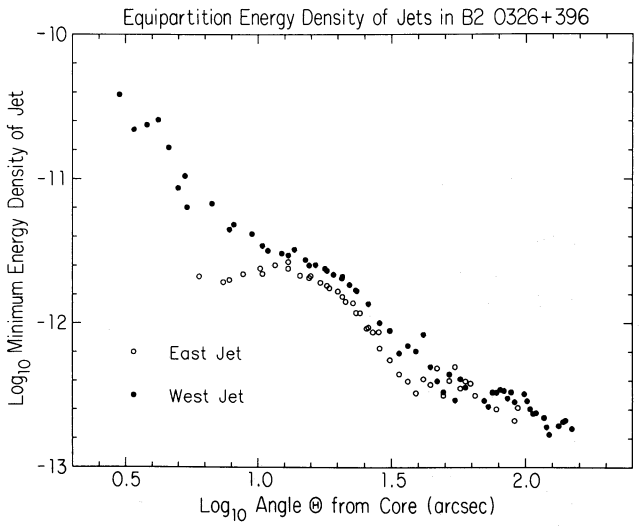

Fig. 14. The minimum energy density U_{eq} in the synchrotron component of the west jet (filled circles) and east jet (open circles), plotted logarithmically against angle Θ from the core

by a single power law. For the west jet beyond $\Theta \approx 8''$ ($2.6h^{-1}$ kpc), $U_{eq} = 10^{-10.84\pm0.09} h^{4/7} d^{-1.16\pm0.04}$ J m^{-3} where d is the projected linear distance from the core in units of h^{-1} kpc. For the east jet $U_{eq} = 10^{-10.92\pm0.11} h^{4/7} d^{-1.19\pm0.10}$ J m^{-3} beyond $\sim 4.5h^{-1}$ kpc from the core. Unfortunately, there are no X-ray data for B2 0326+39 from which to assess the Θ dependence of the external thermal pressure. We therefore cannot determine whether these energy density distributions could be in pressure balance with the hot interstellar medium in the host galaxy.

5.4. *Lateral deviations*

Figure 15 plots the variation of Δ, the deviation of the ridge line of the jets from a line in p.a. 90° through the core, against the angle Θ from the core from the fits to the transverse profiles at 4″ resolution. This plot emphasises the shape of the lateral deflections, also clearly evident in the VLA 6″ × 10″ resolution image in Fig. 5. The jet deflections are *S* symmetric until 50″ ($17h^{-1}$ kpc) from the core, after which the west jet begins to develop the large scale oscillation as it enters its lobe. Estimates of characteristic oscillation wavelengths λ are uncertain as no oscillation can be traced over more than a cycle, but the prominent oscillation in the outer jet around $\Theta = 100''$ has $\overline{\lambda/R_j} = 6.3 \pm 1$, where R_j is the jet radius (taken as $\Phi/2$). The oscillations in the inner jet, near $\Theta = 6''$ (Fig. 10) and $\Theta = 35''$ (Fig. 15) have $\overline{\lambda/R_j} = 11 \pm 1$.

5.5. *Sidedness*

The west jet, which has the bright one-sided knots at its base, is slightly brighter overall. This exemplifies a general relation between initial one-sidedness and large-scale brightness asymmetry that has been found in the jets of other weak radio galaxies (e.g. Bridle 1982). Table 7 lists the sidedness ratio obtained by comparing the integrated flux densities of the jets in the regions where both jets are detectable. These ratios are weighted toward the brightest parts of each region, so they are insensitive to some significant local structure. Figure 16 displays the ratios between the deconvolved peak intensities of the jets as a function of angular distance from the core, from the 4.9 GHz data at 2″ and 4″ resolution. The ratio falls rapidly from its initial lower limits of 7 to 25, reaching 1.2 ± 0.1 near where the east jet achieves its maximum brightness ($\sim 13''$ from the core), then increases to ~ 2 by $\Theta \approx 40''$. At the beginning of the re-expansion in region (4), the sidedness ratio again decreases, i.e., the jet intensities again become more symmetric. Near $\Theta = 50''$ the ratio falls to 0.7 ± 0.1, i.e., there is a short region in which the west jet is fainter than the east. But as the west jet nears the major bend, the brightness ratio increases to about 2.5 ± 0.3. Beyond the bright knot on the outside of the major bend in the west jet about 100″ from the

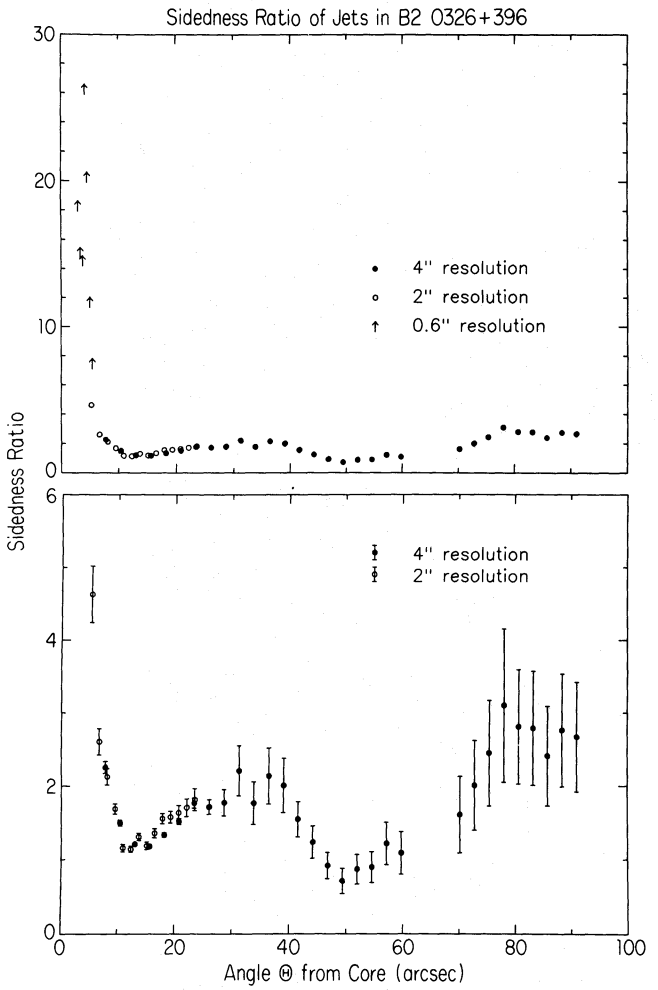

Fig. 16. Sidedness ratio of the jets as a function of distance from the core. (Filled circles – data at 4″ resolution; open circles – data at 2″ resolution; arrows – lower limits at 0.″6 resolution

core, the east jet is hard to identify but the brightness ratio is $\geq 2.5:1$.

5.6. *Spectral properties*

The spectral properties of the jets can be derived from the VLA data at 4″ and 6″ × by 10″ resolution. Figure 17 shows the variation of the spectral index $\alpha_{4.9}^{1.5}$ between 1.5 and 4.9 GHz along the ridge line of the total intensity at 4″ resolution. [We define α so that $S(\nu) \propto \nu^{-\alpha}$.] The index in the bright knots at the base of the jet is unknown, as we cannot resolve them reliably from our 1.5 GHz data. In the west jet, the spectral index steepens from $\alpha_{4.9}^{1.5} \approx 0.36$ about 7″ ($2.4h^{-1}$ kpc) from the core to $\alpha_{4.9}^{1.5} \approx 0.6$ at 17″ ($5.8h^{-1}$ kpc) from the core. It then decreases to 0.35, and increases again to 0.8 about 90″ ($30h^{-1}$ kpc) from the core. Beyond 90″ from the core, the index decreases to about 0.55. In the east jet, the spectral index increases rapidly from 0.36 near its peak brightness about 12″ ($4h^{-1}$ kpc) from the core to 0.82 about 35″ ($12h^{-1}$ kpc) from the core.

The spectral index data at 6″ × 10″ resolution show similar features in the inner 30″ and beyond 60″, but from 30″ to 60″ the indices derived at this resolution are about 0.2 higher than those obtained at 4″ resolution for both jets. This may be evidence for a steeper-spectrum "cocoon" around the jet, and there is some direct evidence for this in the profiles of the spectral index at 4″ resolution transverse to the jet axis. The decrease in the jet spectral index beyond about 90″ from the core is confirmed at this resolution. We note that this decrease begins near the extremum of the major bend in the west jet. This bend may therefore be a region of particle reacceleration near internal shocks induced by the lateral wiggling ("thrashing") of the jet or by interaction with a density inhomogeneity in the ambient medium. The knot is extended at 2″ resolution, however, so if particle reacceleration is occurring here it takes place throughout a region several kpc across.

5.7. *Degree of linear polarisation*

Fig. 18b shows that at 4″ resolution $p_{4.9}$, the degree of linear polarisation at 4.9 GHz, increases rapidly away from the core in both jets. It reaches a peak of $p_{4.9} \sim 0.38$ at $\Theta = \pm 18''$ ($\pm 6h^{-1}$ kpc) from the core, then decreases to <0.2 around $\Theta =$

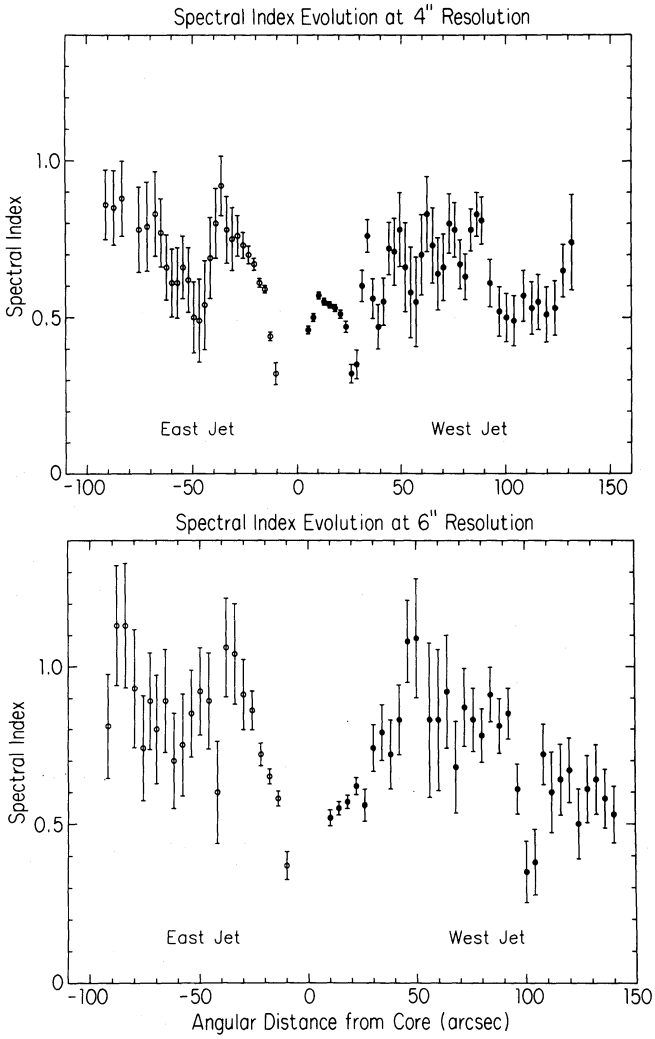

Fig. 17. Variation of the spectral index $\alpha_{4.9}^{1.4}$ and its error along the ridge line of the jets at 4″ and 6″ resolutions

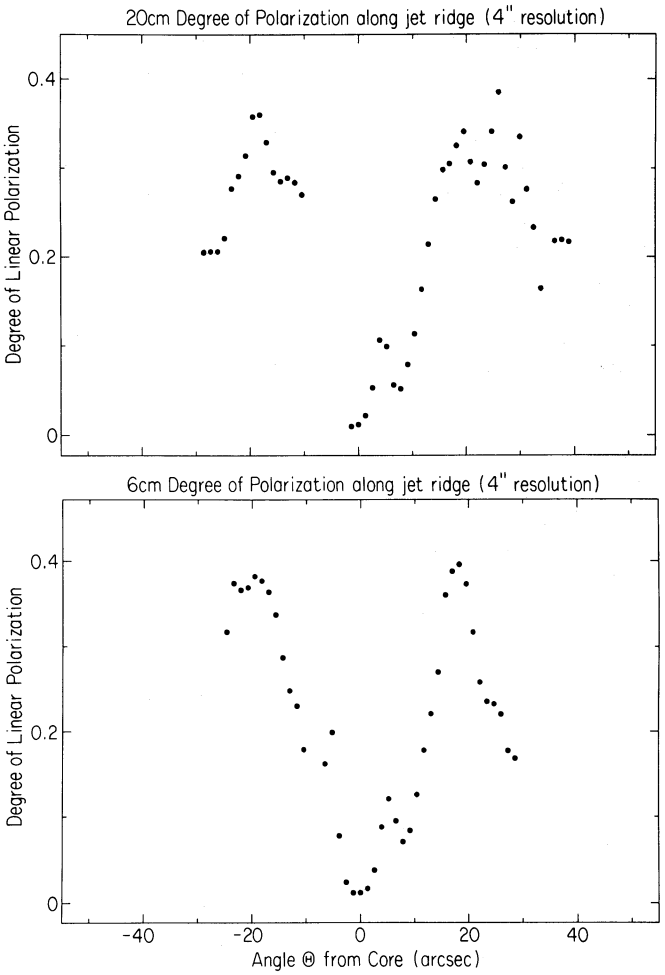

Fig. 18. Variation of the degree of linear polarisation along the ridge line of the jets at 4″ resolution. (Upper panel – λ20cm, 1.4 GHz; lower panel – λ6cm, 4.9 GHz).

30″. The degree of polarisation $p_{1.5}$ at 1.5 GHz, Fig. 18a, tracks that at 4.9 GHz; there is no statistically significant depolarisation between 4.9 and 1.5 GHz at this resolution along the first 30″ of either jet. The data at 6″ by 10″ resolution show that for $\Theta > 30''$ $p_{4.9}$ oscillates between 0.15 and ~0.3 before settling at the higher end of this range as the jets merge with the lobes beyond $\Theta = 100''$.

Figures 18a and b also both show local minima in the degree of linear polarisation of the west jet at $\Theta = 8''$ from the core. These minima mark where the dominant component of this jet's magnetic field changes from being parallel to being perpendicular to the jet axis – see also Fig. 7b and Sect. 5.1(d) above.

The WSRT data show that the jet depolarises significantly between 1.4 and 0.61 GHz. The depolarisation ratio $D_{1.4}^{0.61} = p_{0.61}/p_{1.4}$ is typically from 0.15 to 0.2.

5.8. *Rotation measure (RM)*

The data at 4″ resolution show that the RM increases slightly from east to west across the jets, from $-7 \pm 3\,\mathrm{rad\,m^{-2}}$ at $\Theta = -25''$ ($8.5h^{-1}$ kpc from the core along the east jet) to $0 \pm 3\,\mathrm{rad\,m^{-2}}$ at $\Theta = +25''$ ($8.5h^{-1}$ kpc from the core along the west jet). The internal RM corresponding to the observed jet depolarisation between 0.61 and 1.4 GHz on the simple slab model is $\sim 10\,\mathrm{rad\,m^{-2}}$.

5.9. *Magnetic field configuration*

Figure 19 shows vectors with lengths proportional to the degree of linear polarisation $p_{4.9}$ at 4.9 GHz, and position angles equal to that of the apparent magnetic field (extrapolated to zero wavelength using the observed Faraday RM values) over the first 20″ ($6.8h^{-1}$ kpc) of each jet at 4″ resolution. Note that the ***B*** vectors beyond about 15″ ($5h^{-1}$ kpc) from the core (i.e., after the initial rapid spreading) are not exactly perpendicular to the jet axes – they are significantly oblique at the centerline of the jets, and in the east jet are more oblique south of the centerline, in regions of relatively high linear polarisation. This asymmetric pattern of oblique apparent ***B*** vector directions and high fractional polarisations does not conform to any of the simple axisymmetric 3-dimensional magnetic field configurations that have been used to model jet polarisation data, e.g. Perley et al. (1984). As noted by these authors, oblique field regions are, however, compatible with models that break the axisymmetry.

In the force-free magnetised jet models studied by Königl & Choudhuri (1985), the asymmetry is a fundamental property of the equilibrium field. Regions of oblique field are predicted to be associated with intensity maxima and polarisation minima on the axis (see their Fig. 4) when jets are viewed perpendicularly. They may however be associated with strongly polarised off-axis regions if the jet is viewed obliquely (see their Fig. 5). In the simplest form of their model, the pattern should repeat along the jet and be correlated with intensity knots and with transverse oscillations at intervals of $5R_j \cos \iota$ where ι is the angle between the jet axis and the plane of the sky. There is no evidence for or

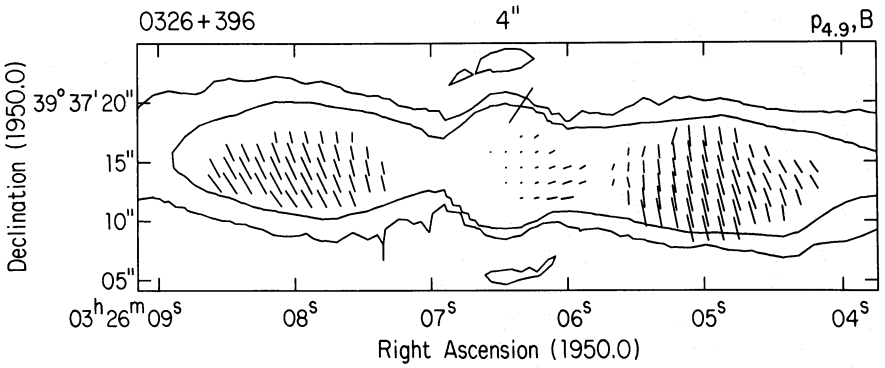

Fig. 19. Vectors showing the degree of linear polarisation $p_{4.9}$ at 4.9 GHz and the position angle of the apparent magnetic field, corrected for the variation of RM across the jet, from the VLA data at 4″ resolution. A vector of length 1″ on the angular scale corresponds to $p_{4.9} = 0.18$

against repetition of the pattern in B2 0326+39, but the observed transverse oscillation wavelengths in the inner jet are at least a factor of two too large to match the prediction of this model.

In the model of Corbelli & Veltri (1989), the radiating particles illuminate only part of a larger-scale field distribution into which they diffuse stochastically. In this model, localised regions of apparently oblique field can arise from the anisotropic pitch angle distribution of the radiating particles. Large-scale regions of uniformly inclined apparent field require a further asymmetry of the relativistic electron distribution relative to the symmetry axis of the currents that generate the fields. The model predicts that the oblique field regions should correlate with asymmetries in the transverse intensity profile. Our data do not obviously match their predictions, but observations at higher transverse resolution are needed to explore this in detail.

6. The lobes

6.1. Integrated properties

Table 8 lists the integrated properties of the lobes derived from the WSRT data. The total spectra of the lobes are similar, but they are steeper than the jet spectra over most of the lengths of the jets. The integrated spectrum of the source, based on single-dish measurements, has a spectral index $\alpha_{4.9}^{1.4} \approx 0.9$. The spectrum of the source below 1.4 GHz is poorly determined; extrapolation of the higher-frequency data to the B2 survey frequency of 408 MHz predicts ~ 5 Jy, but only 1.9 Jy is accounted for by the B2 measurement. At lower frequencies the region is strongly confused by 3C 84, and we know of no reliable measures of the integrated flux density below 408 MHz. There is no evidence from the total spectrum that any significant flux density is missing from the short-baseline interferometer data.

6.2. Spectral properties

Figure 20 displays the spectral indices $\alpha_{1.4}^{0.61}$ between 0.6 and 1.4 GHz and $\alpha_{5.0}^{1.4}$ between 1.4 and 5.0 GHz, from the WSRT data at all three frequencies at $26'' \times 41''$ resolution. At this resolution, the spectra contain a blend of jet and lobe emission until beyond $\sim 60''$ ($20h^{-1}$ kpc) from the core, where the west jet deflects toward the south rim of the west lobe. The west lobe has $\alpha \sim 0.7$ to 0.85 in both frequency ranges beyond $\sim 75''$ from the core, while closer to the core $\alpha_{1.4}^{0.61} \sim 0.9$. The east lobe displays a similar pattern, both spectral indices being in the range 0.6 to 0.8 over most of the lobe, with evidence at the lower frequencies for emission with a steeper spectrum near the core.

The observation that $\alpha_{1.4}^{0.61} > \alpha_{5.0}^{1.4}$ within $\sim 1'$ of the core can be understood if the lobe emission contains a diffuse component with $\alpha \approx 1$, to which the 5-GHz observations are relatively insensitive, and a component with $\alpha \approx 0.6$ to 0.8, similar to the spectrum of the jets. The integrated spectrum of the lobes is indeed steeper than the average of the spectral indices along their major axes, in agreement with this.

The *S* symmetric extensions of the lobes have steep spectra, with $\alpha_{1.4}^{0.61} > 1$. This steep spectrum suggests that these extensions contain an older population of electrons than that in the brighter parts of the lobes, but observations of the spectral curvature and models of the magnetic field evolution in the lobes are required to quantify this statement.

6.3. Polarisation and depolarisation

At 0.61 and 1.4 GHz, the WSRT detects linear polarisation over most of the west lobe and some of the east lobe. The degree of polarisation is more uniform over the lobes at 0.61 GHz, $p_{0.61}$ typically being between 0.02 and 0.1 whereas $p_{1.4}$ ranges from 0.02 to 0.3. Linear polarisation is detected at only a few locations in the lobes on the low resolution 5 GHz WSRT image and on the VLA 1.5 GHz and 4.9 GHz images at $6'' \times 10''$ resolution. In both lobes, the higher degrees of polarisation occur in the regions of lower total intensity, at the edges of the lobes.

The 1.5 GHz VLA data for the east lobe at $6'' \times 10''$ resolution agree well with the WSRT 1.4 GHz results, allowing for the difference in angular resolution. The VLA 1.5 GHz data at this resolution do not show linearly polarised emission from the south rim of the west lobe however, suggesting that the emission with $p_{1.4} \sim 0.1$ to 0.2 on the WSRT image is heavily resolved by the VLA. Curiously, this region is the only part of the west lobe where the VLA detects significant linear polarisation at this resolution at 4.9 GHz, $p_{4.9}$ reaching 0.4 to 0.6. The polarisation structure of the west lobe is evidently more complex than that of the east lobe.

Neither the WSRT nor the VLA data reliably measure the depolarisation between 1.4 and 4.9 GHz in the lobes, because the signal to noise is poor at the upper frequency. In most locations,

Table 8. Integrated parameters of the lobes

	East lobe	West lobe
5.0 GHz flux density	160 mJy	125 mJy
1.4 GHz flux density	530 mJy	510 mJy
0.6 GHz flux density	1130 mJy	1070 mJy
Spectral index	0.95	1.05
10 MHz to 100 GHz luminosity	$4.5\,10^{33}h^{-2}$ W	$4.3\,10^{33}h^{-2}$ W
Angular diameter	$120'' \times 80''$	$120'' \times 80''$
Linear diameter	$41 \times 27h^{-1}$ kpc	$41 \times 27h^{-1}$ kpc
Min. total energy $E_{\min}$	$1.6\,10^{50}h^{-17/7}$ J	$1.8\,10^{50}h^{-17/7}$ J
Min. energy density $U_{\min}$	$1.1\,10^{-13}h^{4/7}$ J m^{-3}	$1.2\,10^{-13}h^{4/7}$ J m^{-3}
Equipartition field B_{eq}	$0.34h^{2/7}\,nT$	$0.36h^{2/7}\,nT$
Depolarisation $D_{1.5}^{0.6}$	~ 0.2	~ 0.4

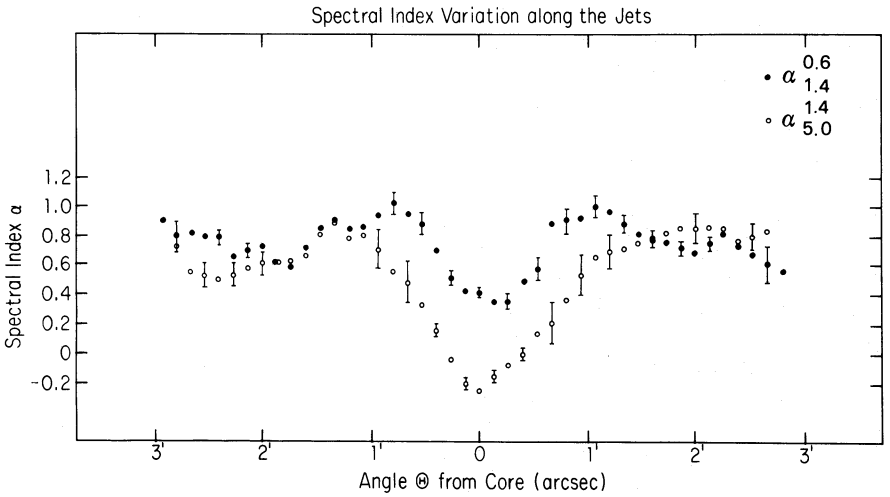

Fig. 20. Spectral indices $\alpha_{1.4}^{0.61}$ between 0.61 and 1.4 GHz (filled circles) and $\alpha_{5.4}^{1.4}$ between 1.4 and 5.0 GHz (open circles) along an east-west cut through the core, from the WSRT data at 26″ × 41″ resolution

they are consistent with $D_{4.9}^{1.4} = p_{1.4}/p_{4.9} \approx 1$, but with errors ≈ 0.4. A notable exception is the emission on the south side of the west lobe, for which $D_{4.9}^{1.4} \approx 0.5 \pm 0.2$.

The depolarisation ratio $D_{1.4}^{0.61} = p_{0.61}/p_{1.4}$ determined from the WSRT data takes values in the range 0.15 to 0.3 over much of the east lobe, rising to ~ 0.5 on its north and east edges. In the west lobe, $D_{1.4}^{0.61}$ is near 1.0 at the center, decreases to 0.15–0.3 on the north edge and to the west, and to 0.3–0.6 to the south. The brighter parts of the two lobes differ significantly in their patterns of depolarisation between the lower frequencies, those of the east lobe being heavily depolarised while those of the west show little depolarisation.

We note that the brighter jet therefore points toward the lobe that is less depolarised, as has been found in the (much more strongly one-sided) jets of powerful (Fanaroff-Riley class II) radio sources by Garrington et al. (1988) and by Laing (1988). The jet velocity regimes estimated for B2 0326+39 in Sect. 7 could not, however, produce the initial brightness asymmetry between these jets by Doppler favoritism.

6.4. *Rotation measure (RM)*

The ***E*** vector rotation can be determined over most of the west lobe between 0.61 and 1.4 GHz with an uncertainty of only a few degrees. It ranges from 50° to 140° ($\pm 180n°$), the average value being $\sim 70° \pm 180n°$. The variations are regular and the largest rotations occur on the south side of the lobe, where the VLA data show the greatest high-frequency depolarisation between these frequencies, however.

The determination of the RM variation across the lobe depends strongly on the scanty 5 GHz polarisation data. The VLA data suggest an RM of $\approx 5\,\mathrm{rad\,m^{-2}}$ in the northern part of the west lobe. The WSRT data in the regions where the 5 GHz polarised intensity is $>5\sigma$ suggest an RM of $26\,\mathrm{rad\,m^{-2}}$ near the centre of the lobe, and a maximum of $\sim 50\,\mathrm{rad\,m^{-2}}$ towards its southwestern edge. The RM gradient cannot however be determined unambiguously from these data, because of residual ambiguities in the value of n at different locations in the lobe. The WSRT data are more consistent with $n = 1$, whereas the VLA data suggest $n = 2$. The uncertainty of $\Delta n = 1$ corresponds to $\Delta\mathrm{RM} = 16\,\mathrm{rad\,m^{-2}}$.

In the east lobe, there are fewer data from which to determine the RM, but using points where the 0.61 and 5 GHz polarisation are significant at the 5σ level, we find a mean RM of $0\,\mathrm{rad\,m^{-2}}$. The VLA 1.5 GHz and 4.9 GHz data at 6″ × 10″ resolution confirm this general trend, showing that the more highly polarised parts of the east lobe 155″ to 175″ from the core have RMs ranging from $-2\,\mathrm{rad\,m^{-2}}$ to $-12\,\mathrm{rad\,m^{-2}}$, the RM tending to be more negative further east in the lobe.

All of the polarisation data therefore suggest that there are RM gradients across the source, from about $-12\,\mathrm{rad\,m^{-2}}$ in the east lobe about 160″ from the core to $\sim 5\,\mathrm{rad\,m^{-2}}$ on the northern side of the west lobe about 120″ from the core and $\sim 50\,\mathrm{rad\,m^{-2}}$ on the south edge of the west lobe, about 180″ from the core. The RM gradient might therefore be as large as $60\,\mathrm{rad\,m^{-2}}$ over $\sim 5'$ across B2 0326+39, i.e. about $60\,\mathrm{rad\,m^{-2}}$ over $100h^{-1}$ kpc if the Faraday screen is at the distance of the radio galaxy.

The significant difference in mean RM between the two lobes resembles the result for 3C 382 and 3C 386 by Strom et al. (1978). The RM gradient across 3C 382 is about twice that across B2 0326+39 in terms of $\mathrm{rad\,m^{-2}}$ per arc minute, but would be similar in terms of $\mathrm{rad\,m^{-2}}$ per kpc if both screens are at the distances of the radio galaxies. It is not clear, however, whether the screen in front of B2 0326+39 is associated with the radio galaxy or with the foreground medium in our galaxy. The galactic co-ordinates of B2 0326+39 are $l = 153°.1$, $b = -13°.6$. There are eight other extragalactic sources within 15° of this position whose integrated rotation measures are known. Their RM's have a wide dispersion, from -136 to $+339\,\mathrm{rad\,m^{-2}}$.

6.5. *Magnetic field configuration*

The distribution of the magnetic field directions in the lobe, estimated from the WSRT 1.4 GHz data after correcting for the Faraday rotation measure gradients, is sketched in Fig. 21. The VLA 4.9 GHz polarisation data confirm this field morphology wherever the signal to noise ratio of the polarised emission is sufficiently high at this frequency. The uncertainty of $\Delta n = 1$ in the rotation angle corresponds to an uncertainty in the individual ***B*** vectors of 40° when converting from 1.4 GHz, but the corrections from 4.9 GHz are $\leq 10°$ everywhere. The magnetic field in the lobes is tangential to the edges, like that in 3C 219 and 3C 353

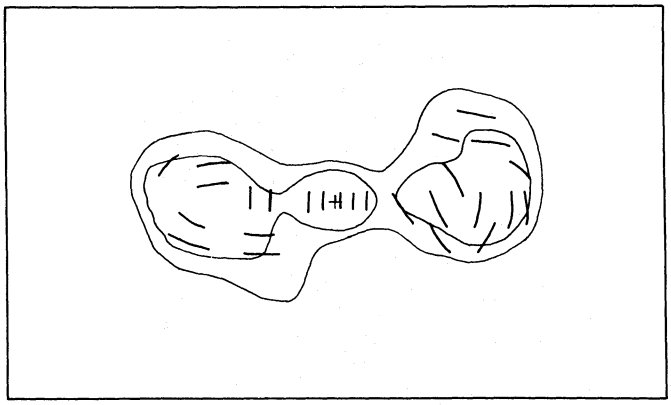

Fig. 21. Sketch of the magnetic field configuration in the large-scale lobe structure, derived from the WSRT 1.4 GHz data after correction for the Faraday RM gradient across the lobes.

(Fomalont 1972; Perley et al. 1980) and other sources with relaxed lobes (e.g. 3C 310 – van Breugel 1980; van Breugel & Fomalont 1984; 3C 382 and 3C 386 – Strom et al. 1978). This apparent field configuration can be achieved in tangled-field models like that of Laing (1980, model C) or if the lobe fields are generated by passively expanding a jet field that has both axial and toroidal organised components (Clarke et al. 1989).

7. Discussion

7.1. Summary of jet properties

The jets can be divided into five major regions characterised by different spreading rates and different intensity-radius evolution. We have also found that these regions have different spectral and polarisation properties. Their properties are collected in Table 7.

In the first region, within 5″ of the core, the west jet is much brighter than the east jet, its apparent magnetic field is parallel to the jet axis, and its brightness distribution is dominated by a few "knots". The jet dims, and its radius, spectral index and degree of linear polarisation increase rapidly with distance from the core.

In the next 13″, the jet spreading rate decreases from the large value achieved near $\Theta = 5''$; the west jet dims relatively slowly while the east jet rapidly brightens. The apparent magnetic fields in both jets become predominantly perpendicular to their axes. The spectral indices of both jets continue to increase, and their degrees of polarisation increase rapidly, reaching values near 0.38.

For the next 22″, both jets expand slowly and their brightness declines rapidly while the degree of polarisation falls to about 0.15. The spectral index of the west jet oscillates while increasing on average, while that of the east jet increases steadily. The west jet begins a large-scale oscillation that is unparalled in the east jet. In both jets, the intensity becomes poorly correlated with their radii.

At the northward extremum of the oscillation of the west jet, its brightness increases and its spectral index decreases by about 0.3. By this distance from the core, the east jet, which was spreading more slowly, has become hard to distinguish from the lobe.

To compare the observed intensity-radius evolution with theoretical benchmarks, we refer to the laminar-jet "adiabats" that correspond to the following assumptions: (a) magnetic flux is conserved, (b) the radiating particles do work as the jet both expands laterally and responds to variations in its flow velocity v_j, (c) there is no particle reacceleration, (d) the relativistic electron energy spectrum is a power law of index γ from energies E_{min} to $E_{max} \gg E_{min}$, and (e) the jet is optically thin. Then for a well-resolved jet dominated by $B_{\parallel}$, the peak intensity

$$I \propto A_j^{-(5\gamma+7)/6} l_j v_j^{-(\gamma+2)/3} \tag{2a}$$

where A_j is the jet's cross-sectional area and l_j is its depth along the line of sight; for $B_{\perp}$-dominated fields, the relation is

$$I \propto A_j^{-(\gamma+2)/3} l_j^{-(\gamma-1)/2} v_j^{-(5\gamma+7)/6} \tag{2b}$$

(e.g. Bridle 1986).

For circular jets with $A_j = \pi R_j^2$ and $l_j = R_j$ these "laminar adiabats" become $I \propto R_j^{-(5\gamma+4)/3} v_j^{-(\gamma+2)/3}$ for $B_{\parallel}$ dominant, and $I \propto R_j^{-(7\gamma+5)/6} v_j^{-(5\gamma+7)/6}$ for $B_{\perp}$ dominant. For a circular jet with $\alpha = 0.6 \pm 0.2$, the energy index $\gamma = 2.2 \pm 0.4$ so

$$I \propto R_j^{-5.0\pm0.7} v_j^{-1.4\pm0.1} \tag{3a}$$

if $B_{\parallel}$ dominates, or

$$I \propto R_j^{-3.4\pm0.5} v_j^{-3.0\pm0.3} \tag{3b}$$

if $B_{\perp}$ dominates.

Region (3) of the observed $I(\Phi)$ behaviour ($I \propto \Phi^{-4.4\pm1.1}$) approximates the slope of both $I(R_j)$ laminar adiabats [Eqs. (3a) and (3b)] for a *constant-velocity* circular jet. The other regions all exhibit much flatter $I(\Phi)$ relations. They must either depart significantly from the assumptions that underly the adiabats, or they must be subject to rapid longitudinal deceleration. For example, the required decelerations would be $v_j \propto R_j^{-0.3\pm0.4}$ in region (1) of the west jet, or $v_j \propto R_j^{-0.9\pm0.1}$ in region (2) of the same jet.

7.2. Mach number and velocity estimates

7.2.1. Velocity from spectral ages

If there is no particle reacceleration in a jet, any *protracted* spectral steepening with distance from the core can be interpreted as ageing of the relativistic electron spectrum by synchrotron losses. If the magnetic field is assumed to be at its equipartition strength, such spectral "ageing" can be assigned a time scale using, for example, the calculations of Myers & Spangler (1985). The angular scale of the spectral gradient and the spectral "age" then imply a parametric velocity, $v_{\Delta\alpha}$. This exceeds the true velocity v_j in the jet if there is particle reacceleration, and may either over- or under-estimate it if the field is significantly out of equipartition.

Our data for B2 0326+39 show spectral gradients of both signs in different parts of the jet. They also contain some local "detail" that probably stems from inexact deconvolution, especially in the relatively poor-quality 1.5-GHz VLA data. Estimates of $v_{\Delta\alpha}$ for this source are therefore not particularly robust. The longest segment of steadily increasing spectral index occurs in regions (2) and (3) of the east jet. Here, the spectral index increases from 0.36 to 0.82 between $\Theta = 12''$ ($4h^{-1}$ kpc) and $\Theta = 35''$ ($12h^{-1}$ kpc). As the average equipartition magnetic field strength $\overline{B_{eq}}$ in this region is $11h^{2/7}$ μG, this gradient corresponds to $v_{\Delta\alpha} = 430\ h^{-4/7}$ kms^{-1} for the east jet $\sim 8h^{-1}$ kpc from the core using the constant pitch-angle (KP) assumption of Myers & Spangler. For their isotropy-seeking (JP) case, the same observational data yield $v_{\Delta\alpha} = 500h^{-4/7}$ km s^{-1}. For the west jet in region (2),

the spectral index increases from 0.45 to 0.6 between $\Theta = 7''$ ($2.4h^{-1}$ kpc) and $\Theta = 17''$ ($5.8h^{-1}$ kpc), where $\overline{B_{eq}} = 19h^{2/7}$ μG. These parameters give $v_{\Delta\alpha} = 540h^{-4/7}$ km s^{-1} $\sim 3.7h^{-1}$ kpc from the core in the KP case, and $v_{\Delta\alpha} = 650h^{-4/7}$ km s^{-1} in the JP case. The apparent steepening of the west jet spectrum from an index of 0.5 to 0.7 at $30'' < \Theta < 50''$, where $\overline{B_{eq}} = 8.3h^{2/7}$ μG, yields $v_{\Delta\alpha} = 310h^{-4/7}$ km s^{-1} $\sim 14h^{-1}$ kpc from the core in the KP case, $v_{\Delta\alpha} = 410h^{-4/7}$ km s^{-1} in the JP case.

These estimates of v_j cannot be taken as rigorous upper limits, however. The underlying assumption of equipartition is questionable. The apparent spectral gradients also depend on resolution and are not monotonic, as they would be if they were produced entirely by spectral ageing. These estimates do illustrate, however, that relatively low velocities are consistent with explaining the larger spectral gradients in this jet by synchrotron losses if the fields are near their equipartition strengths.

7.2.2. Mach number from lateral oscillations

The lateral oscillations of the jets could in principle be ascribed to various causes. These include orbital, precessional or other semiperiodic motions of the parent object, and growing Kelvin-Helmholtz instabilities on the jet boundary. Orbital motions alone should produce a single oscillation wavelength λ with fixed oscillation amplitude Δ and ***C*** symmetry between the jets (e.g. Blandford & Icke 1978). The major oscillation of the west jet clearly grows with distance from the core and there is no sign of a ***C***-symmetric oscillation in the east jet, so we discard this hypothesis for B2 0326+39. Precessional motion alone should produce a single oscillation whose amplitude Δ grows linearly with Θ and displays ***S*** symmetry between the jets. This is harder to rule out, because the amplitude of the terminal oscillation of the west jet grows approximately as $\Delta = 0.1\Theta$ and the lobes and inner parts of the jets exhibit an overall ***S*** symmetry. It could be argued that the east jet is simply too faint for our data to test the *geometrical* symmetry required by this interpretation.

Interpreting the transverse oscillation as a growing Kelvin-Helmholtz instability on a confined jet is qualitatively attractive, but several difficulties beset the comparison between theoretical calculations and observed oscillation wavelengths. Theoretical calculations of the fastest growing instability wavelengths are made in the linear regime whereas instabilities that become large enough to modify the appearance of a jet are clearly nonlinear. Theory also predicts the *fastest-growing* wavelength for any given instability, whereas the observations emphasize the wavelength with the *largest amplitude* in any given region of the jet. These need not be identical. Despite this, numerical models of *slab* jet propagation in the nonlinear regime have shown that the wavelengths of the largest oscillations are close to those predicted by linear analysis (Norman & Hardee 1988). It is therefore interesting to explore the general regime of Mach number that could lead to the observed behaviour.

Hardee (1987) shows normalised curves of the wavelength λ_1 of the fastest growing helical or sinusoidal ($n = 1$) distortion of a supersonic pressure-confined *cylindrical* jet against its internal Mach number $\mathcal{M}_j$ and density contrast $\eta = p_j/p_e$, the ratio between the densities in the jet and in the external medium. These curves, derived from a spatial-domain perturbation analysis, are approximated at high $\mathcal{M}_j$ by the expression:

$$\lambda_1 \approx \frac{5.2\mathcal{M}_j R_j}{0.66 + \eta^{1/2}}. \qquad (4)$$

For $\mathcal{M}_j < 3$, Eq. (4) over-estimates the resonant oscillation wavelengths by 25% to 50%. The *minimum* internal Mach number $\mathcal{M}_j$ associated with a given oscillation wavelength corresponds to $\eta \to 0$, for which Eq. (4) becomes $\mathcal{M}_j \to 0.13\lambda_1/R_j$ at high Mach numbers. In the highly-entrained limit $\eta \to 1$, Eq. (4) gives $\mathcal{M}_j \to 0.32\lambda_1/R_j$ at high Mach numbers.

For the large-amplitude oscillation of the outer west jet around $\Theta = 100''$, the observed $\overline{\lambda/R_j} = 6.3 \pm 1$. This outer oscillation could not therefore comply with the theoretical assumption of $\mathcal{M}_j > 1$ if $\eta \to 0$. If, however, the jet had entrained enough ambient gas to make $\eta \approx 1$ by $\Theta \approx 100''$, the oscillation could be a helical Kelvin-Helmholtz mode with $\mathcal{M}_j \sim 3.0$ (based on the curve given by Hardee for this regime of $\mathcal{M}_j$). The formal error in this estimate of the Mach number would be ± 0.3, but this is probably optimistic.

Closer to the core, at $\Theta = 35''$ we observe an oscillation with $\overline{\lambda/R_j} = 11 \pm 1$, which can be satisfied in the low-density ($\eta \to 0$) limit for $\mathcal{M}_j \to 1.7$. In the bright base of the west jet, the lateral oscillation following the bright knot has $\lambda = 2''.5$. The FWHM Φ increases so rapidly in this region that $\overline{R_j}$ is ill-defined and the theoretical assumption of slow jet spreading is questionable, however. We estimate that $5 < \overline{\lambda/R_j} < 11$, consistent with helical oscillations of a jet with $1 < \mathcal{M}_j \leq 1.7$ if $\eta \ll 1$ initially.

We therefore infer that *mildly supersonic flow* ($\mathcal{M}_j$ between 1.7 and 3) and *outwardly increasing density contrast* η are together consistent with the observed oscillation wavelengths if these are attributed to growing fluid dynamic instabilities.

7.2.3. Mach number from knot spacings

Prandtl (1904, 1907) obtained the relation $\lambda = 2.61R_j\sqrt{\mathcal{M}_j^2 - 1}$ for the natural wavelength λ between weak shocks in a mildly supersonic jet. Killeen & Bicknell (1988) use this relation to estimate the Mach number in the jets of IC 4296 from the interknot spacing λ_k in a train of regularly spaced knots. The Prandtl relation has only a limited range of applicability, however–both laboratory data and numerical simulations show saturation at $\lambda \approx 4R_j$ as the shocks strengthen. Norman et al. (1985) showed from simulations of pressure-confined jet propagation at higher Mach numbers ($3 < \mathcal{M}_j < 6$) that saturated reflection modes yield shock "diamond" spacings $\lambda_k = (4.9 \pm 0.3)R_j$ with little sensitivity to $\mathcal{M}_j$ or η in this range. Our MEM image (Fig. 10) suggests that $3.5 < \lambda_k/R_j < 4.8$ in the base of the west jet at $\Theta < 5''$. If the knot spacing here indeed corresponds to the geometry of oblique shock "diamonds", the base of the jet must be near the saturation regime of Prandtl's formula. This is weak evidence for $1.8 \leq \mathcal{M}_j \leq 3$ in the west jet near the core. The lower end of this range is consistent with the Mach number estimated above from the lateral oscillations in this region.

7.2.4. Mach number from spreading rate

The Mach number of a *free* jet where it detaches from its confinement can be estimated from $d\Phi/d\Theta = (2/\mathcal{M}_j)\sec\iota$ where ι is the angle between the jet axis and the plane of the sky. The slow intensity-radius decline over most of the jets in B2 0326+39 implies that they are not spreading freely, but the best candidate for a freely-spreading region would be the initial rapidly-spreading region where the jet energy density declines rapidly with Θ. The *fastest* spreading rate in this region, $d\Phi/d\Theta = 0.41$, corresponds to $\mathcal{M}_j = 4.9 \sec\iota$. If the jet is confined in this region, the sound speed would exceed the observed expansion speed, in which

case this approach would over-estimate the true internal Mach number at entry to the jet base.

It has also been suggested (Bicknell 1986a) that the general anticorrelation between turbulent stress and Mach number may link the spreading rates of confined turbulent jets to $\mathcal{M}_j$ at low Mach numbers. Too many factors may be at play to use this relationship to estimate $\mathcal{M}_j$ in any one jet, however. The spreading rates of turbulent laboratory jets depend not only on $\mathcal{M}$, but also on the internal energy density U_{int}, and on conditions in the initial boundary layer as measured by the initial Strouhal number (e.g. Lau 1981; Gutmark & Ho 1983). Elliptical jets also spread at different rates on their minor and major axes (Gutmark et al. 1988).

7.2.5. Velocity from lobe energetics

Bicknell (1986a) has pointed out that if the thermal contribution to the pressure in a jet is neglected, one may estimate the flow velocity from energy balance without knowing the thermal particle density in the jet. The energy flux F_e along the jet is

$$F_e = \pi R_j^2 v_j \left(\frac{1}{2}\rho_j v_j^2 + P_{int} + U_{int}\right) \tag{5}$$

where ρ_j is the particle density, P_{int} is the total internal pressure,

$$P_{int} = \frac{B^2}{8\pi} + \frac{1}{3}U_{rel} + nkT \tag{6}$$

and U_{int} is the total internal energy density

$$U_{int} = \frac{B^2}{8\pi} + U_{rel} + \frac{3}{2}nkT. \tag{7}$$

If $nkT \ll U_{rel}$ and $\ll B^2/8\pi$, the thermal density can be eliminated from the expression for the energy flux using the relation

$$\rho_j v_j^2 = \frac{4}{3}P_{int}\mathcal{M}_j^2. \tag{8}$$

Bicknell assumes that U_{rel} dominates all other terms, but we make the usual equipartition assumptions and put $B^2/8\pi = 3U_{rel}/4$, so that

$$\begin{aligned} F_e &= \frac{34}{13}\pi R_j^2 v_j P_{int}\left(1 + \frac{13\mathcal{M}_j^2}{51}\right) \\ &= \frac{34}{21}\pi R_j^2 v_j U_{int}\left(1 + \frac{13\mathcal{M}_j^2}{51}\right). \end{aligned} \tag{9}$$

Equation (9) is the equipartition (minimum-energy) analogue of Eq. (3.5) of Bicknell (1986a). If the lobe derives all of its energy from the jet, then

$$F_e = \frac{L_{lobe}}{\kappa}, \tag{10}$$

where L_{lobe} is the lobe luminosity, $\kappa = \tau/t_{rad}$ while the age τ of the source is much less than the mean radiative lifetime t_{rad} of the particles in the lobe, and $\kappa \to 1$ if radiative equilibrium is reached.

The neglect of nkT in Eqs. (6) and (7) is encouraged by several general arguments that many jets are light, i.e. that $\eta = \rho_j/\rho_e \ll 1$. First, it is common for radio galaxies whose luminosities are just above the boundary between FR classes I and II to have lobes that are much wider than their jets. Wide lobes form when the velocity of advance of the hot spots, v_{hs}, is much less than the jet velocity v_j. Momentum balance then requires $\eta \ll 1$. It would be surprising if the jets in FR I sources that are only a little less luminous than these wide-lobed doubles have much higher initial values of η. Second, numerical modeling of jet bending (Williams & Gull 1984; Williams 1985) has shown that heavy bent jets exhibit surface instabilities that conflict with observations of the radio "trail" sources, whereas light jets do not. O'Dea (1985) also concluded from general arguments that the jets in narrow trails should be light. Neglect of nkT is therefore reasonable provided the minimum energy density U_{min} estimated from equipartition is not too low and the temperature T is not too high. We examine these constraints quantitatively for B2 0326+39 later.

For the inner west jet, where the surface brightness is greatest and neglect of nkT should be best, we find, using Bicknell's "top-hat" approximation for which $R_j^2 = \Phi_j^2/3$, that the velocity v_j estimated by the above method varies along the jet. If the jet stays in equipartition, $v_j \propto \Phi^{-10/7} I^{-4/7}$ (apart from the minor effects of changes in the Mach number and spectral index), so the velocity estimate is constant only if $I \propto \Phi^{-2.5}$. Regions of slower brightness decline are necessarily ones in which the *estimate* of v_j from Eq. (9) decreases, and those of faster decline are ones in which the estimate increases, with distance from the core. Writing $v_j = v_{j0} h^{-4/7}\kappa^{-1}\left(1 + \frac{13\mathcal{M}_j^2}{51}\right)^{-1}$, we find that the "scaling velocity" v_{j0} decreases from 8200 km s^{-1} at the base of region (1) ($\Theta = 3''$) to a local minimum of 450 km s^{-1} by the end of region (2) ($\Theta = 18''$), then returns to $\sim$900 km s^{-1} by the end of region (3). For most of regions (2) and (3), $v_{j0} = 750 \pm 250$ km s^{-1}. A second decrease in v_{j0} occurs as the jet brightens and expands near $\Theta = 60''$, and $v_{j0} \sim 180 \pm 50$ km s^{-1} for $\Theta > 90''$.

7.2.6. Conclusions

The above discussion suggests that the jet is a pressure-confined flow whose Mach number $\mathcal{M}_j \lesssim 3$ over most of its length, and whose velocity v_j decreases while the density contrast η increases with increasing distance from the core. If the jet is confined, the (high) Mach number estimated from its spreading rate is an upper limit. The Mach number range (1.8 to 3) estimated from the spacing of the initial bright knots is slightly greater than that ($\sim$1.7) estimated from the initial lateral oscillations using Hardee's (1987) spatial stability analysis, but the discrepancy is well within the uncertainties in both estimates.

If $\mathcal{M}_j \sim 1.7$ through most of regions (2) and (3), the lobe energetics [Eqs. (9) and (10)] give $v_j = 430 h^{-4/7}\kappa^{-1}$ km s^{-1} if the thermal energy and pressure in the jet are small. This estimate of the velocity would be consistent with that from the spectral gradients if $\kappa \sim 1$ in Eq. (10), but we show below that such a high value of κ corresponds to an excessive Faraday depth in the outer jet. If $\mathcal{M}_j \sim 3$ in region (4), as suggested by the lateral oscillation of the outer west jet, $v_j = 55 h^{-4/7}\kappa^{-1}$ km s^{-1} there.

The estimated Mach number and velocity can be used to infer the thermal number density n_j via Eq. (8) if we also assume that the pressure P_{int} in the jet is near its equipartition value and that the typical heavy particle is a proton. For $\Theta = 10''$, we obtain $n_j = 2.3\,10^{-2} h^{12/7}\kappa^2$ cm^{-3} and for $\Theta = 100''$, $n_j = 3.6\,10^{-1} h^{12/7}\kappa^2$ cm^{-3}.

If the magnetic field strength is near its equipartition value *and* the mean line-of-sight field is $B_{los} = B_{eq}/\sqrt{3}$, the Faraday depth of the jet would be $200\kappa^2 h$ rad m^{-2} at $\Theta = 10''$, and

$6000\kappa^2 h$ rad m^{-2} at $\Theta = 100''$. Our RM and depolarisation data show that any RM associated with the jet is ≤ 10 rad m^{-2}. The Faraday depth constraint for $\Theta = 100''$ therefore makes it highly unlikely that $\kappa \sim 1$ in Eq. (10), i.e. the lobes are unlikely to have reached radiative equilibrium with the rate of energy supply from the jets. Although in principle B_{los} can be much less than $B_{eq}/\sqrt{3}$ if there are many field reversals along the line of sight, it is more likely that $\kappa \leq 0.04$.

For $\kappa = 0.04$, the jet parameters at $\Theta = 10''$ would be $v_j = 10{,}000h^{-4/7}$ km s^{-1}, $n_j = 3.7\,10^{-5}h^{12/7}$ cm^{-3}, and those at $\Theta = 100''$ would be $v_j = 1400h^{-4/7}$ km s^{-1}, $n_j = 6\,10^{-4}h^{12/7}$ cm^{-3}. With these parameters, the neglect of nkT in Eqs. (6) and (7) is reasonable for $\Theta = 10''$ if $T < 3\,10^9$ K, and for $\Theta = 100''$ if $T < 4\,10^7$ K. These temperatures are high enough that they are unlikely to be exceeded in any way other than by the jet reaching thermal equilibrium with the relativistic particles (in which case $nkT \sim U_{rel}$ and the velocity estimates would be slightly decreased). Our estimates of jet velocity and Mach number imply sound speeds in the jet of $250h^{-4/7}\kappa^{-1}$ km s^{-1} near $\Theta = 10''$ and $18h^{-4/7}\kappa^{-1}$ km s^{-1} near $\Theta = 100''$. In ionized hydrogen and with $\kappa = 0.04$, these correspond to temperatures of $1.8\,10^9 h^{-8/7}$ K and $9.4\,10^6 h^{-8/7}$ K respectively. The inner jet may therefore be closer to the regime in which the correction for the thermal energy is significant.

The velocities estimated above using $\kappa = 0.04$ are much greater than those implied by the observed spectral gradients (Sect. 7.2.1a) if the magnetic fields and relativistic particles are in equipartition. The discrepancy could imply either that the magnetic field strengths in the jets are above their equipartition values or that analysing the *steepest* apparent spectral gradients systematically under-estimates $v_{\Delta\alpha}$. The apparent complexity of the spectral index structure in this jet casts some doubt on the velocity estimates from spectral ageing, while the lack of depolarisation and RM structure in the outer jet argues strongly against high values of κ or magnetic fields that are much stronger than their equipartition values. Because of the discrepancies between the spectral indices we obtained at different resolutions (see Figs. 17 and 20), we give greater weight to the higher velocities derived from the energy budget.

7.3. *The jets as turbulent mixing regions*

In region (3), where both jets spread only slowly, the central intensity declines rapidly with increasing jet radius. The regions of faster jet spreading correspond to more moderate intensity-radius decline or to *brightening* of the jets. This general anticorrelation between spreading rate and the rate of intensity-radius decline has been observed in the well-resolved jets in several other weak radio galaxies with powers below $10^{24.5}h^{-2}$ W Hz^{-1} at 1.5 GHz (Henriksen et al. 1982; Morganti et al. 1987). Arguments such as those used above usually estimate internal Mach numbers in the range $1 < \mathcal{M}_j < 3$ for the jets in such sources (Bicknell 1985). The lobes of such sources also lack well-defined "working surfaces" – the jets become meandering plumes and "trails" rather than ending at well-defined bright "hot spots" as in more powerful sources. This is evidence that the *final* Mach numbers of their jets are generally low. As the estimated Reynolds numbers are high ($\sim 10^{11}$, e.g. Henriksen et al. 1982), it would be surprising if such jets are not turbulent.

The anticorrelation between spreading rate and intensity-radius decline could arise from two types of physical process in turbulent jets at low Mach number. First, entrainment of ambient gas across the boundary layer of a rapidly spreading turbulent jet will reduce the longitudinal velocity v_j (and maintain or increase the density contrast η). Where the jet magnetic field is predominantly perpendicular to the axis, longitudinal compression of the field and particles can moderate the intensity-radius law for the jet, whether or not particles are reaccelerated along the jet. This effect was first discussed by Fanti et al. (1982) and it has since been analysed in detail by Bicknell (1985; 1986a,b). Second, the regions of rapid spreading are also the most likely sites for relativistic particle reacceleration driven by Lighthill radiation from fully developed MHD turbulence. This process was outlined by Henriksen et al. (1982) and has been modelled in detail by Eilek & Henriksen (1984). Both effects may make mildly supersonic turbulent jets fade slowest where they spread fastest, as observed.

Bicknell (1986b) suggests that adiabatic deceleration by entrainment can explain the observed brightness of extensive regions of the jets in the giant radio galaxy NGC 315 without further appeal to particle acceleration, if those jets are also reaccelerated and recollimated by buoyancy at the appropriate radius. He interprets the region of rapid jet spreading as one of turbulent entrainment and slowdown, and the recollimation region as a reversion to laminar flow at increased Mach number, driven by the pressure gradient in the atmosphere of NGC 315. Bicknell's model has recently been successfully applied to a sample of 23 jets in 15 low-luminosity radio galaxies (Bicknell et al. 1990).

B2 0326+39 and NGC 315 are almost identical in radio power, and the ranges of spreading rates in their jets are similar. We have therefore tried to model our brightness data for B2 0326+39 using Bicknell's precepts. Note however that the linear scales of all the jet phenomena in NGC 315 are larger than those in B2 0326+39. The recollimation shoulder begins at $35h^{-1}$ kpc in NGC 315 compared with $6h^{-1}$ kpc in B2 0326+39, and the overall size of NGC 315 is $820h^{-1}$ kpc compared with $115h^{-1}$ kpc for B2 0326+39.

The models were fitted as follows. First, for the west jet, a spline curve was fitted to the $\Phi(\Theta)$ data out to $\Theta = 120''$ as shown in Fig. 22. Lacking X-ray or optical data on the gravitational potential in the host galaxy, we assumed a $\beta \approx 1$ atmosphere in a King model, and then adjusted β and the core radius R_c to find a fit. It was not possible to fit the brightness data at $\Theta < 20''$ well using the model, but satisfactory fits were obtained for $\Theta > 20''$. The other panels of Fig. 22 show the best fit obtained to all of the data. Acceptable fits were obtained from models with $0.003 < \eta < 0.02$, $0.8 < \beta < 0.9$, gravitational potential constant $W_0 \sim 9.5$, core radius in the range $1.5 < R_c < 2.5h^{-1}$ kpc and $\mathcal{M}_j \sim 1$ to 4. The range for each parameter has been obtained by determining the values for which the reduced χ^2 exceeds its minimum value by one. The data for the east jet can be reproduced (as shown in Fig. 23) by models with $0.34 < \eta < 0.69$, $0.9 < \beta < 1.5$, gravitational potential constant $W_0 \sim 9.5$, core radius in the range $1.0 < R_c < 3.0h^{-1}$ kpc and $\mathcal{M}_j \sim 1$ to 4. We were unable to fit both jets satisfactorily with common values of the parameters, however. In all cases, much higher density contrasts η were required to fit the data for the east jet.

We cannot therefore duplicate Bicknell's detailed success with NGC 315 when applying his model to *the full length* of the jets in B2 0326+39. The main difference between NGC 315 and B2 0326+39 in this context is that the initial brightness decline

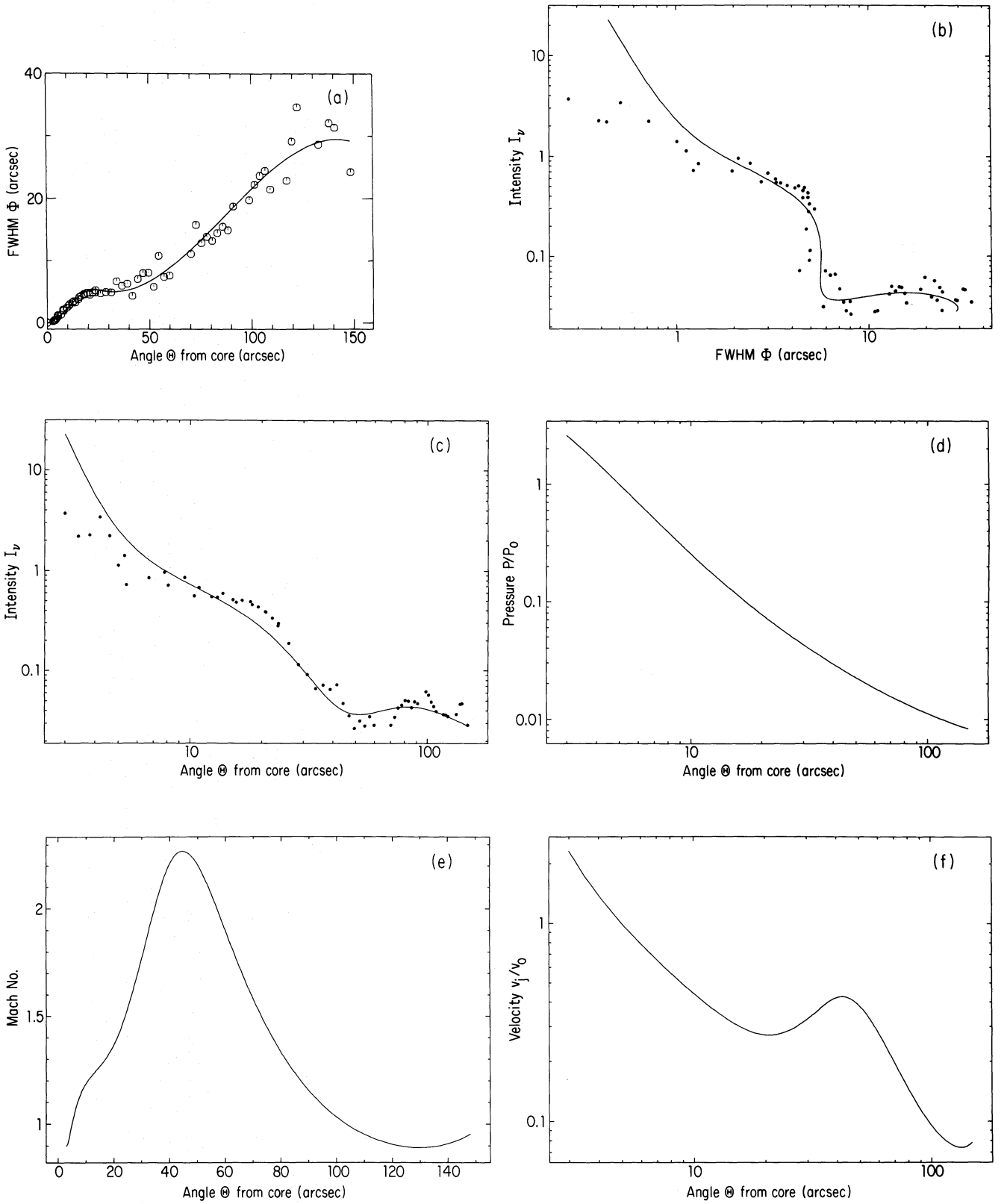

Fig. 22. a Spline fit to the $\Phi - \Theta$ collimation data for the west jet. **b – f** Results of fitting a Bicknell (1986b) model with $\beta = 0.8$, $R_c = 2.0$ kpc, $W_0 = 9.5$ and initial jet parameters $\eta = 0.004$ and $\mathcal{M}_j = 1.0$. **b** shows the predicted $I - \Phi$ (intensity-width) variation (solid line) and the data from Fig. 12. **c** shows the predicted $I - \Theta$ (intensity-distance) variation (solid line) and the data. **d** is the fitted $P - \Theta$ (pressure-distance) variation for the background medium. **e** shows the predicted variation of the jet Mach number $\mathcal{M}_j$ with distance Θ. **f** is predicted variation of jet velocity v_j with Θ. Subscript '0' indicates a parameter value taken at a fiducial point in the jet – we have used the point where the magnetic field makes its transition from dominantly-parallel to dominantly-perpendicular to the jet axis

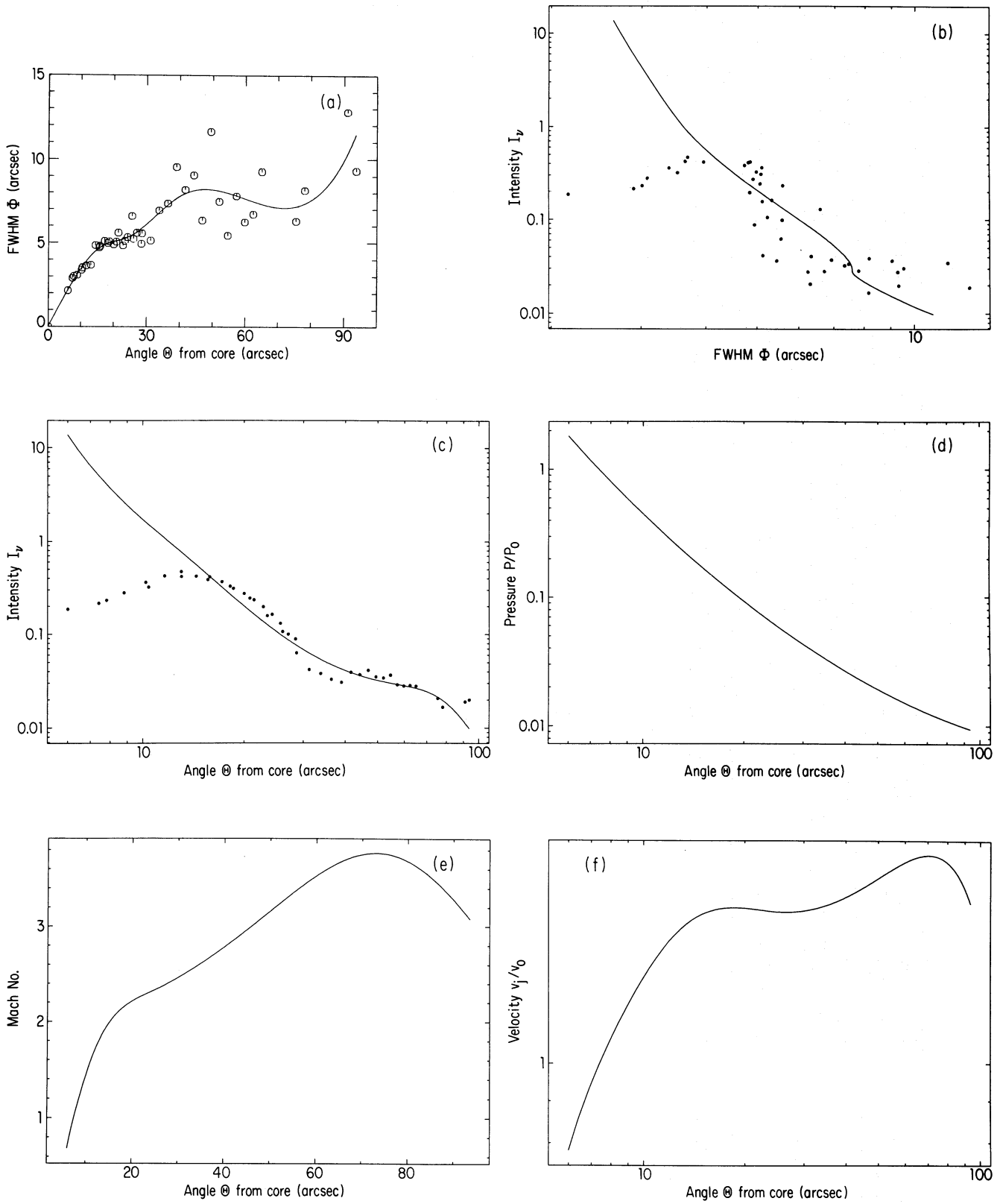

Fig. 23. a Spline fit to the $\Phi - \Theta$ collimation data for the east jet. **b – f** Results of fitting a Bicknell (1986b) model with $\beta = 1.3$, $R_c = 1.0$ kpc, $W_0 = 9.5$ and initial jet parameters $\eta = 0.48$ and $\mathcal{M}_j = 1.0$. **b** shows the predicted $I - \Phi$ (intensity-width) variation (solid line) and the data from Fig. 12. **c** shows the predicted $I - \Theta$ (intensity-distance) variation (solid line) and the data. **d** is the fitted $P - \Theta$ (pressure-distance) variation for the background medium. **e** shows the predicted variation of the jet Mach number $\mathcal{M}_j$ with distance Θ. **f** is the predicted variation of jet velocity v_j with Θ. Subscript '0' indicates a parameter value taken at a fiducial point in the jet – we have used the point where the magnetic field makes its transition from dominantly-parallel to dominantly-perpendicular to the jet axis

in much faster in NGC 315 and so conforms better to the expectations of the model. Furthermore, in Bicknell's picture, the recollimation region would be a phase of laminar "adiabatic" flow followed by re-expansion to a more turbulent jet. One might then expect a higher degree of linear polarisation in the recollimation region (Bicknell 1986b). This is not observed. We also note that the Mach number variation obtained from the model fit (Fig. 22e) exceeds what is needed to explain the lateral oscillations as Kelvin-Helmholtz instabilities.

We conclude that *the general* $(\mathcal{M}_j, v_j, \eta)$ *regime proposed by Bicknell seems appropriate for the jets* in B2 0326+39, but more sophisticated models appear to be needed to describe their properties fully. The jets in B2 0326+396 have mixed properties–a large spreading rate (a common characteristic of less powerful sources) but bright knots at the base of the jet [a common characteristic of more powerful sources for which the description given by Bicknell's model is not completely adequate (Bicknell et al. 1990)]. We should also seek models that can account for (a) the initial one-sidedness of the jets, (b) their re-brightening where they begin to bend, and (c) the general correlation between "one-sidedness" in jets segments and the dominance of the $B_{\parallel}$ projected magnetic configuration (Bridle 1982).

A radically different relationship between jet morphology and brightness has been proposed by Corbelli & Veltri (1989). These authors develop the suggestion by Benford et al. (1980) that the morphology of radio jets reflects a spatial cross-field diffusion of the relativistic particles mediated by MHD turbulence. In their model, the spreading of the radio jet reflects only the diffusive spreading of relativistic electrons injected near the base of the jet, not the spatial spreading of the magnetic field. The relativistic electrons merely "light up" more of the jet field distribution further from the core. In this model, the magnetic flux conservation embodied in the "standard adiabats" is incorrect, because the field strength is governed not by the spreading of the relativistic electrons but by that of the thermal current density that supports the fields. If the field strength B is thereby decoupled from the synchrotron jet radius R_j, the "adiabats" in Eq. (2) become

$$I \propto (A_j v_j)^{-(2+\gamma)/3} l_j \tag{11}$$

for either $B_{\parallel}$ or $B_{\perp}$. For a circular jet with $\alpha = 0.6 \pm 0.2$ and $\gamma = 2.2 \pm 0.4$,

$$I \propto R_j^{-1.8 \pm 0.3} v_j^{-1.4 \pm 0.1} \tag{12}$$

in the Corbelli-Veltri model. Although Eq. (12) specifies a slower variation of I with R_j than the "standard" adiabats in Eq. (3), the flow would still have to decelerate initially, with $v_j \propto R_j^{-0.5}$, for Eq. (12) to match the $I(\Phi)$ behaviour observed in regions (1) and (2). Region (3) could be interpreted as the transition to a constant width of the synchrotron emitting region relative to that of the field distribution (the usual assumption), and regions (4) and (5) would require particle reacceleration.

In the Corbelli-Veltri model, the correlation between jet sidedness and apparent field configuration near the base of the jet arises naturally from the anisotropic pitch angle distribution of the radiating particles relative to the field. The rapid spreading in region (1) could produce the apparent transition in the magnetic field orientation by illuminating regions of azimuthal field away from the core of the jet without decreasing the net field strength. The streaming particles would also acquire velocities directed away from the jet axis, reducing the initial brightness asymmetry between the jet and the counterjet. Detailed polarisation and intensity profiles at high angular resolution could test this model.

Acknowledgements. We thank Geoff Bicknell for numerous discussions about modelling turbulent jets. Stefi Baum thanks the NRAO for the award of a summer studentship during which much of the calibration and imaging for this project was completed.

References

Baars J.W.M., Hooghoudt B.G., 1974, A&A 31, 323
Benford G., Ferrari A., Trussoni E., 1980, APJ 241, 98
Bicknell G.V., 1985, in: Physics of Energy Transport in Extragalactic Radio Sources, Proc. NRAO Workshop No. 9, eds. A.H. Bridle, J.A. Eilek, NRAO: Green Bank, 229
Bicknell G.V., 1986a, APJ 300, 591
Bicknell G.V., 1986b, APJ 305, 109
Bicknell G.V., de Ruiter H.R., Fanti R., Morganti R., Parma P., 1990, APJ 354, 98
Blandford R.D., Icke V., 1978, MNRAS 185, 527
Bridle A.H., Henriksen R.N., Chan K.L., Fomalont E.B., Willis A.G., Perley R.A., 1980, APJ 241, L145
Bridle A.H., 1982, in: Extragalactic Radio Sources, Proc. I.A.U. Symp. 97, eds. D.S. Heeschen, C.M. Wade, Reidel, Dordrecht, P. 121
Bridle A.H., 1984, AJ 98, 979
Bridle A.H., 1986, Can. J. Phys. 64, 353
Burns J.O., Feigelson E.D., Schreier E.J., 1983, APJ 273, 128
Clarke D., Norman M.L., Burns J.O., 1989, APJ 342, 700
Colla G., Fanti C., Fanti R., Gioia I., Lari C., Lequeux J., Lucas R., Ulrich M.-H., 1975, A&AS 20, 1
Corbelli E., Veltri P., 1989, APJ 340, 679
Eilek J.A., Henriksen R.N., 1984, APJ 277, 820
Ekers R.D., Fanti R., Lari C., Parma P., 1981, A&A 101, 194
Fanti C., Fanti R., Gioia I.M., Lari C., Parma P., Ulrich M.-H., 1977, A&AS 29, 279
Fanti R., Fanti C., Parma P., Bridle A.H., Ekers R.D., Fomalont E.B., 1982, A&A 110, 169
Feretti L., Giovannini G., Gregorini L., Parma P., Zamorani G., 1984, A&A 139, 55
Fomalont E.B., 1972, Astrophys. Lett. 12, 187
Fomalont E.B., Bridle A.H., Willis A.G., Perley R.A., 1980, APJ 237, 419
Garrington S.T., Leahy J.P., Conway R.G., Laing R.A., 1988, Nat 331, 147
Gutmark E., Ho C.-M., 1983, Phys. Fluids 26, 2932
Gutmark E., Schadow K.C., Wilson K.J., Bicker C.J., 1988, Phys. Fluids 31, 2524
Hardee P.E., 1987, APJ 313, 607
Henriksen R.N., Bridle A.H., Chan K.L., 1982, APJ 257, 63
Högbom J.A., 1974, A&AS 15, 417
Högbom J.A., Brouw W.N., 1974, A&A 33, 289
Killeen N.E.B., Bicknell G.V., Ekers R.D., 1986, APJ 302, 306
Killeen N.E.B., Bicknell G.V., 1988, APJ 324, 198
Königl A., Choudhuri A.R., 1985, APJ 289, 173
Laing R.A., 1980, MNRAS 193, 439
Laing R.A., 1988, Nat 331, 149
Lau J.C., 1981, J. Fluid Mech. 105, 193
Myers S.T., Spangler S.R., 1985, APJ 291, 52

Morganti R., Fanti C., Fanti R., Parma P., de Ruiter H.R., 1987, A&A 183, 203
Napier P.J., Thompson A.R., Ekers R.D., 1983, Proc. IEEE 71, 1295
Norman M.L., Smarr L., Winkler K.-H.A., 1985, in: Numerical Astrophysics, eds. J.M. Centrella, J.M. LeBlanc, R.L. Bowers, Jones & Bartlett, Boston: P. 88
Norman M.L., Hardee P.E., 1988, APJ 334, 80
O'Dea C.P., 1985, APJ 295, 80
O'Dea C.P., Owen F.N., 1986, APJ 301, 841
Parma P., 1982, in: Extragalactic Radio Sources, Proc. I.A.U. Symp. 97, eds. D.S. Heeschen, C.M. Wade, Reidel, Dordrecht, P. 193
Parma P., Fanti C., Fanti R., Morganti R., de Ruiter H.R., 1987, A&A 181, 244
Perley R.A., Willis A.G., Scott J.S., 1979, Nat 281, 437
Perley R.A., Bridle A.H., Willis A.G., Fomalont E.B., 1980, AJ 85, 499
Perley R.A., Bridle A.H., Willis A.G., 1984, APJS 54, 291
Prandtl L., 1904, Phys. Zeit. 5, 599
Prandtl L., 1907, Phys. Zeit. 8, 23
Saunders R., Baldwin J.E., Pooley G.G., Warner P.J., 1982, MNRAS 197, 287
Schwab F.R., 1980, SPIE Proc. 231, 18
Strom R.G., Willis A.G., Wilson A.S., 1978, A&A 68, 367
Thompson A.R., Clark B.G., Wade C.M., Napier P.J., 1980, APJS 44, 151
van Breugel W.J.M., 1980, A&A 81, 265
van Breugel W.J.M., Fomalont E.B., 1984, APJ 282, L55
van Someren Gréve H.W., 1974, A&AS 15, 343
Williams A.G., Gull S.F., 1984, Nat. 310, 33
Williams A.G., 1985, Ph. D. Thesis, University of Cambridge
Willis A.G., Strom R.G., Birdle A.H., Fomalont E.B., 1981, A&A 95, 250